The page and line numbers used in the response are referring to the revised manuscript, which is appended to this response. Note that this is not the final revised manuscript, but is provided to show the reviewers where we made changes to address their concerns.

Anonymous Referee #1

Received and published: 26 November 2019

General comments

This paper describes an analysis of solar broadband and spectral irradiance data from an airborne measurement campaign in the Arctic in September 2014. Comparisons were made with radiative transfer model calculations (RTM) that take into account concurrent cloud products from MODIS satellite observations and retrievals of local spectral surface albedos from the aircraft measurements. A significant fraction of the work is concerned with the determination of the spectral ground albedos taking into account measured upwelling and downwelling irradiances, video images from the ground and literature data in spectral ranges where measurements were not feasible. The effort is justified because under the Arctic conditions, accurate ground albedos are crucial to distinguish cloud radiative effects from the influence of the relatively bright snow- or ice covered surface.

In general, the agreement of measurements and RTM calculations is satisfactory for both broadband and spectral measurement (at two selected wavelengths). However, significant differences were observed during some periods where no clouds were present according to the satellite data. This is taken as a hint towards the presence of undetected, optically thin clouds. However, in my view this interpretation is not as clear as currently presented in the paper and the influence of experimental uncertainties requires more attention. Nevertheless, the paper is well written, structured and documented. It should be published after minor revision.

R: Thank you very much for your comments, especially for bringing up experimental uncertainties. We didn’t appreciate until reading the reviewers’ comments how central to the manuscript the uncertainty analysis is (see below).

To make the interpretation of the study more clear and to avoid confusion in the revised manuscript, we 1) modified the aim of this paper in the introduction (see **Line 14, Page 4**); 2) added a detailed description for each step of our approach at the beginning of the Data and Methods section (**see Line 5, Page 5**); 3) removed the discussion of cloud radiative effects that can be derived from the upwelling and downwelling irradiance.

We agree that the uncertainty analysis, which was missing in the original manuscript, was crucial because it can not only affect the conclusions drawn in the paper but can also help to make the conclusions stronger. We made an effort to add the uncertainty analysis for 1) the snow fraction estimated from nadir camera imagery; 2) the SSFR-BBR combined irradiance product; 3) the radiative transfer calculations based on MODIS cloud products to the revised manuscript (see **Appendix D, Line 12, Page 17**). We revised the figures by adding in the uncertainties as error bars as well as the text in the results discussion. Although the figures and the manuscript changed after adding in the uncertainty analysis, the conclusions of the paper did not change.

Specific comments

Page 2, line 10: Clarify “radiative transfer model” instead of “model”

R: Thank you. We corrected to “… inter-comparisons of irradiance measurements and radiative transfer calculations” (see **Line 10, Page 2**).

Page 2, line 15: “. . .about 22% of clouds remained undetected (cloud optical thickness less than 0.5).” This statement is not in agreement with the main text, see page 11, line 36.

R: Thank you for noticing the typo. We corrected the percentage in the result discussion (**Line 13, Page 13)** to make the statement consistent with the abstract. Also, the reviewer suggested to count the undetected clouds differently. As a result, the percentage number changed, but the numbers are kept consistent throughout the revised manuscript.

Page 3, line 14: “ . . .every 10^6 km^2 decrease. . . a 2.5 W m^{-2} increase“. The statement is unclear. For which area does this apply?

R: To make it more clear, we added the area information “averaged over the region from 75 ° N to 90 ° N” (**Line 15, Page 3**) to make the statement more clear.

Page 4, line 36: Give more information on the flight area, altitudes and times e.g. in the text, in a table or a modified Fig. 1.

R: We modified the Figure 1 by adding the longitude, latitude and altitude information. In addition, we specified the region in the figure caption.

Page 5, line 16: The broadband instruments were probably not actively aligned. That should be made clear. Were data excluded from the analysis when the aircraft attitude was not horizontal?

R: The broadband instrument (BBR) was not actively aligned. No, the data is not excluded when the aircraft attitude was not horizontal. A software attitude correction (Long et al., 2010) was applied to the BBR data to account for the change of solar position due to aircraft pitching and rolling. We added clarifications in the revised manuscript (**see Line 16, Page 5**).

Page 5, line 25: “. . . that keeps the zenith light collector horizontal. . .“ I assume that both collectors were actively aligned. If so, that should be clearly stated because for the determination of net irradiances this is certainly important.

R: No, only the zenith light collector was actively aligned. The nadir light collector was fix mounted at the bottom of the aircraft. We added clarifications in the revised manuscript (see **Line 36, Page 5**).

Page 5, line 28: “. . . that cannot be corrected.” Another reason why low sun elevations are more challenging for the downwelling direct irradiance is that the gradient d cos(SZA) / (d SZA) increases with SZA.

R: This is an excellent point. We think we have addressed this point in the original manuscript by mentioning “This is particularly important in the Arctic, where low sun elevations lead to large systematic errors for fix-mounted or poorly stabilized sensors (Wendisch et al., 2001)” (see **Line 37, Page 5**).

Page 6, line 9: ". . . atmospheric effects". You probably mean "collector effects"?

R: The "atmospheric effects" was misleading, but we didn't mean "collector effects". We meant the effect of cirrus. We modified to text to "… atmospheric effects (e.g., cirrus)" (**Line 21, Page 6**) to clarify.

Page 6, line 25: I am convinced that the complicated collector-specific corrections and calibrations were done thoroughly. But can you estimate the remaining uncertainties for the upwelling and downwelling measurements, both broadband and spectral? For example in Appendix B, Fig. 13 the scatter in the ratios indicates uncertainties of the independently calibrated instruments that will not vanish by applying the azimuth correction. I assume Fig. 13 shows downwelling irradiances? If so it would be interesting to see a similar plot for the upwelling (with similar scatter but no azimuth dependence).

R: Thank you for pointing out the lacking uncertainty estimation – and see above our response. Specifically for this comment: Yes, we made a considerable effort to add a thorough error analysis for the upwelling and downwelling, broadband and spectral irradiance measurements and calculations in the revised manuscript (see **Line 12, Page 17**).

BBR was more accurate (3% accuracy), but SSFR had spectral resolution, as described above. SSFR's azimuthal response was not isotropic (unlike BBR's), and it was corrected with BBR's response during a dedicated calibration flight. After azimuthal correction, the SSFR downwelling irradiance was scaled to BBR using the method described in Appendix D. It is in this sense that SSFR and BBR data were "merged". However, they are not identical. Since the calibration flight and the science flight occurred at different sun-sensor geometries, the broadband irradiance derived from SSFR and measured by BBR may deviate slightly from each other. We show them both to check for consistency between both methods. We need to show SSFR (in addition to just BBR) because we later use spectral irradiances from SSFR only to draw conclusions.

The details can be found in the revised manuscript Appendix D (see **Line 12, Page 17**). Yes, Fig. 13 shows downwelling irradiance. Figure A2 shows a plot of wavelength-integrated SSFR irradiances vs BBR. The linear relationship of upwelling irradiance indicates no azimuth response in upwelling irradiance.

Page 6, line 36, Eq. 1: The different weighing implies a conversion to "brightness" or "luma" rather than a (relative) physical radiance. The source of the three coefficients should be cited and what they represent.

R: The weighting conversion we used was to convert RGB colors from the video to "brightness". The nadir camera was not radiometrically calibrated, thus it could not provide any physical radiance for this study. Thank you for your suggestion, we added the reference as a footnote for the conversion weights (see **Line 14, Page 7**).

Page 7, line 15: ". . .robust estimates". I wonder what robust means. The procedure is quite complicated and there are obviously several sources of uncertainties: (1) the coefficients in Eq. 1, (2) the blending technique Eq. 2, (3) the adaptive thresholding (parameters given in Appendix C) and (4) the (presumably) limited field of view of the camera compared to the irradiance collector. For example, does it make a significant difference if 0.333 is inserted in Eq. (1) for R, G, and B? It

would be convincing if you could provide an uncertainty estimate for the snow fraction based on a sensitivity study taking into account the different aspects (1)-(4).

R: Thank you for the detailed thoughts on this matter. We used "robust estimates" because the method provides a reasonable snow fraction for the nadir camera images (even for scenes of pure snow) inspected by the human eye. The word "robust" can be subjective so we decided to delete the sentence to avoid confusion. We added an uncertainty analysis for the snow fraction estimated from the nadir camera images. The analysis shows that (1) and (2) were minimal factors compared to (3) and (4). We applied different FOV sizes and different adaptive thresholding areas and used the standard deviation of snow fraction retrieved using different parameter combinations of (3) and (4) to represent the estimate of snow fraction uncertainties. We included text regarding these sources of uncertainty to the revised manuscript (see **Line 34, Page 17**).

Page 8, lines 12 and 13: Exchange hygrometer and thermometer in 3) and 4) Page 8, equation (4): Why not define "α_{SSFR} =" here?

R: Thank you for pointing this out. We exchanged hygrometer and thermometer at **Line 32, Page8** and defined α_{SSFR} in Equation (4) at **Line 24, Page 9**.

Page 9, line 6: I assume the atmospheric correction was comparatively small because the altitude was below 300 m? You should give the reader a rough idea.

R: Thank you for your suggestion. Yes, the atmospheric correction was comparatively small. The atmospheric correction corrected less than 0.2% on flight level albedo at the non-absorbing wavelengths. We added the magnitude information in the revised manuscript (see **Line 32, Page 18**).

Page 9, line 33: To support this statement you could include the (much lower) albedo of the open ocean in Fig. 5. Moreover, in the introduction you mention a climatological surface albedo for the region by Moody et al., 2007 that is used for the MODIS cloud retrievals. It would be interesting to see how this compares with the locally measured data.

R: Thank you for your suggestions. The spectral shape of the albedo that we obtained from our parameterization indicates that the surface albedo of the dark endmember (snow fraction of 0) consists of dark ice instead of open ocean, and the nadir camera imagery supports that. As supplementary material, we provide a video for the flight track that we used the aircraft data to do the spectral albedo parameterization (see supplementary material S1 "s1_flight-video_20140913-clear-sky.mp4"). Thus, we decided to not include the open ocean surface albedo.

We agree that the albedo used for the MODIS 1621 cloud retrievals is helpful, so we included it in Fig. 6.

Page 10, line 9: Why 70%? In Fig. 4 a majority of data points is well above 80%.

R: The 70% was determined by matching the radiative transfer calculations with the upwelling irradiance measured by SSFR-BBR at 1640 nm under clear-sky (~ 0.0107 $Wm^{-2}nm^{-1}$). After adding the uncertainty analysis for snow fraction estimated from nadir camera image, the surface albedo parameterization changed. As a result, when we tried to match the clear-sky calculations with the clear-sky measurements, the snow fraction we got from the new surface albedo parameterization was 76.4%.

The data used to come up with the parameterization of the surface albedo in Fig. 4 is only a small portion of the data collected on 2014-09-13 (below-cloud under clear-sky) because only a small portion from this case was collected under clear-sky conditions. The majority of the clear-sky data points in Fig. 4 does indeed have a snow fraction well above 80%, but the conditions for the entire region conducted on 2014-09-11 (a different day/location) are different, and we did not know what was the exact snow fraction was. We arrived at a snow fraction of 76.4% by tweaking the clear-sky calculations until they matched the clear-sky measurements at 1640 nm (we added an explanation how we arrived at this number in the revised manuscript, **Line 38, Page 10**).

Page 10, line 21: "cloud optical thickness"

R: Thank you for noticing the typo. We corrected to "cloud optical thickness" (see **Line 20, Page 11**).

Page 10, line 21: ". . .agree with measurements within 10%" Does this statement refer to data in Fig. 7b or to other flight periods? In Fig. 7b agreement within 10% under no-cloud conditions is only visible at the very beginning. My impression is that good agreement during periods where no clouds were detected could be reached by increasing the snow fraction to about 80% without significantly affecting the upwelling in the presence of clouds. So the 70% snow fraction assumption and its uncertainty are crucial here and should be discussed.

R: Yes, the 10% statement was referring to Fig. 7b. As we discussed in the previous response at "Page 10, line 9: ….", the 70% was determined by matching the radiative transfer calculations with the upwelling irradiance measured by SSFR-BBR at 1640 nm under clear-sky (~ 0.0107 $Wm^{-2}nm^{-1}$). We agreed that by adjusting the snow fraction to a higher value would increase the calculation-measurement consistencies in general, however, the nadir camera imageries indicate very thin clouds (wavy patterns) existed. Later, we used the multi-pixel approach (see Fig. 12) and found the surface albedo changed spectrally that the surface albedo parameterization we obtained from 2014-09-13 clear-sky data cannot perfectly represent the surface albedo of 2014-09-11 by adjusting the snow fraction. We added the uncertainty analysis for the snow fraction and associated uncertainty in radiative transfer calculations in the revised manuscript (see **Line12, Page 17**).

Page 10, line 23: ". . . below 0.5" In Fig. 7b it seems that the missing about 30 W m^{-2} upwelling RTM irradiance (above the clear baseline) correspond to a missing COT of about 2 which is well above the threshold of 0.5. Moreover, if the COT were indeed around 2 no ice-structures on the ground would be visible in the photographs (i)-(iv).

R: Due to the dense collection of the data points, the COT threshold was not clear. We did evaluate the histograms of the irradiance and the 30 Wm^{-2} low bias in the upwelling calculations was associated with the missing COT of about 0.5.

Page 10, line 23: The ". . . continuous variation from leg to leg. . ." Compared to the COT data the measured peaks in the upwelling irradiance look smoothed out. I wonder if this has to do with the fields of view of the instruments which at 7 km altitude are much greater than that of the satellite (1 km). So even if you fly above a correctly detected cloud gap, the sensors could receive irradiance from surrounding, even distant cloud fields. So, overall wonder if the results in Fig. 7 can be explained without "undetected clouds", i.e. by field of view effects and an underestimated albedo.

R: These are excellent thoughts. Indeed, the FOV size is greater than that of satellite and the clouds from surrounding or distant area can contribute signals in upwelling irradiance, and we now added a discussion regarding this point (see **Line 23, Page 11**). However, our conclusions were drawn based on the following two points (1) With a 45º Field Of View (FOV), the FOV size is much smaller than the cloud gap; (2) from the time-synched images from the nadir camera, thin clouds were clearly seen beneath the aircraft where MODIS identified as clear-sky. The primary factor that we base our conclusion on is (1). To support our point that the FOV is smaller than the cloud gaps, we added horizontal error bars in Fig. 7b. Overall, the size of these horizontal error bars adds uncertainty to the percentage number of clouds that go undetected by MODIS, but the general statement (that MODIS under-detects low-level thin clouds) is still supported by our data. The nadir imagery (2) further supports makes our statement more plausible because we can actually see clouds. The camera imagery thus does not serve as quantitative estimation of the amount of clouds that are missed, but simply corroborate our findings in a qualitative way.

Page 11, line 3: “. . . via the snow fraction” What was the mean snow fraction during that flight?

R: The mean snow fraction during that flight (2014-09-13 below cloud case) was 91.6%.

Page 11, line 7: “. . .except. . .22:22:48” I cannot find that period in the figure.

R: The 22:22:48 was in the format of HH:MM:SS for Fig. 8 (a) and (b).

Page 11, line 11: “. . . no evidence of any cloud gap”. This also hints towards different fields of view of satellite and aircraft. Even if you fly underneath a cloud gap, at estimated solar zenith angles of around 70 deg no direct radiation (and a corresponding increase of irradiance) may be present. It may be detected at other places (also underneath a cloud) but the chances for that are low if the cloud gap is small and cloud thickness is substantial. It would be helpful to estimate the size of the cloud gaps detected by the satellite. Moreover, a statement should be included whether or not the cloud top and bottom heights were correctly retrieved from the satellite data on both days.

R: The reviewer is right; from the below-cloud observations one cannot actually make a strong statement. That is because the satellite is viewing the scene from above (potentially overhead), whereas the change in irradiance as seen from the aircraft is dominated by the direct beam, which can easily be blocked by clouds even if there are gaps (because of the low sun elevation and cloud geometrical thickness). We overlooked this because our impression and understanding of the clouds came from the nadir and forward camera videos that were not included in the manuscript. We attached the flight video we created (synchronized the forward, nadir camera) for this particular flight track (see supplementary material S1 “s1_flight-video_20140913-clear-sky.mp4”). The video confirms that clouds were geometrically thin, and that there were indeed gaps, or very thin clouds with the blue sky shining through as shown on the left figure. From the MODIS perspective, the scale of these cloud gaps or very thin cloud segments is most likely below the pixel dimension (1km). The MODIS cloud detection algorithm seems to interpret these features as gaps, as shown on the map to the right (figure titled “Cloud Optical Thickness”). These occur right on the flight track we analyzed (thick black line), for example, near -133.5°, 73.1°. The size of the gaps in the MODIS L2 retrievals range from 1km to 3km as shown to the

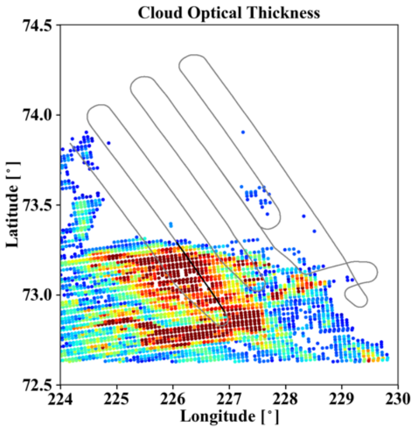

right, but in reality, the gaps (or very thin clouds) as shown on the picture occur on much smaller spatial scales.

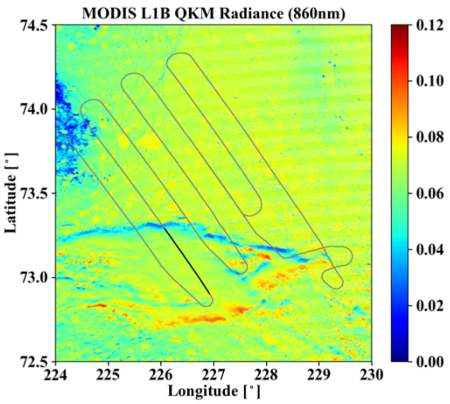

After thinking about the two figures included here, we no longer think that the different sun-sensor geometry explains the fact that cloud gaps show up in the MODIS-based calculations, but not in the measurements. Instead, we now believe that small cloud gaps or thin clouds do occur in the measurement area, but they have different effect on the aircraft observations relative to the satellite observations. **From the below-cloud perspective, the gaps (or very thin clouds) are not large or frequent enough permit the direct beam to be transmitted, leading to an irradiance time series that looks fairly smooth. From the satellite perspective, several sub-grid resolution gaps seem to prevent the detection of a cloud at that pixel.** These undetected pixels in the middle of an otherwise fairly homogeneous cloud field (COT 5-6) can be regarded as an artifact. In that sense, MODIS does "miss" these pixels. We surmise that this happens not because the optical thickness is below some threshold (as in the other case), but because of sub-grid variability of the cloud field. The figure on the left (figure titled "MODIS L1B QKM Radiance (860nm)") shows the radiance field at the finest spatial MODIS resolution (0.25 km). It shows a multi-pixel cloud gap (blue color near the northern end of the thick black line). It does not show any real cloud gaps south of that, unlike the L2 retrieval above, which does show some gaps. We added a brief explanation in the manuscript (see **Line 19, Page 12**).

Page 11, line 15: Table 1 and 2 contain a main result of this study that is not adequately discussed here and should clearly enter the abstract and conclusions: Under conditions when clouds are detected the numbers in the first three columns agree, at least (I assume) within experimental uncertainties which need to be specified.

R: We acknowledge that we did not adequately discuss the cloud radiative effect shown in Table 1 and 2. In the revised manuscript, we decided to focus on the irradiance comparison. Thus we removed Table 1 and 2. In addition, we added uncertainties. They are provided for both the measurements and calculations and indicated as error bars in the updated figures of the revised manuscript.

Page 11, line 23: Do September 11 and 13 belong to the Arctic dry or wet season?

R: Based on the definition in Kay and L'Ecuyer's (2013) paper, September 11 and 13 are belong to dry season. In the revised manuscript, we added the comparison for the dry- and wet-season albedo with the surface albedo derived for September 11 in Figure 6.

Page 11, line 36: "Of all pixels along . . . 22%" To determine the fraction of undetected clouds as stated in the abstract, green/(cloudy +green) should be calculated.

R: Thank you – this is a great idea and more suitable for representing "percentage of undetected clouds". We recalculated the percentage using green/(cloudy+green) and we got 27%. We revised the 22% to 27% using your proposed method throughout the revised manuscript.

Page 11, line 37: ". . . (highlighted in green) are actually cloudy." Again the question arises if during the green periods clouds were undetected by the satellite or radiation was captured unintentionally by the irradiance sensors at some distance from the aircraft.

R: Thank you for your insightful thoughts. You are correct – the large field of view (FOV) of the aircraft radiometers (when flying high) will capture irradiance by clouds at some distance from the aircraft. To evaluate this, we assumed a FOV of 45° for the radiometer and calculated the FOV size based on the aircraft altitude. The FOV is defined as the cone from within which 50-70% of the radiation originates (of course, radiation from the entire hemisphere is detected, but it is weighed much less for incidence angles much larger than 45°). Roughly speaking, the diameter of the SSFR "pixel" size corresponding to the 45° (>half-power) FOV equals the altitude of the aircraft above the cloud deck. Accounting for the motion of the aircraft, we translated the FOV size (units: meter) to time (units: second) and showed the diameter of the FOV along the flight track as horizontal error bars in Fig. 7b. We added an explanation in the revised manuscript (see **Line 23, Page 11**). The horizontal error bars show that the region of undetected clouds is much larger than the FOV effect. The nadir camera imagery also supports this because the clouds can be clearly seen directly below the aircraft. Thus, our conclusions of ". . . (highlighted in green in Figure 9b) are actually cloudy." is correct, even after considering the FOV effect.

Page 12, line 19: ". . . surface albedo ... is biased low by about 9%". The 9% come from the albedo + atmospheric correction which is probably significant at 7 km altitude.

R: The atmospheric correction would not affect the percentage (e.g., 9%) because we were comparing the upwelling irradiance from the SSFR-BBR and radiative transfer calculations at flight altitude. The atmospheric effects were considered in the radiative transfer model (RTM). However, the cirrus will contribute to the percentage because we didn't consider cirrus in the RTM.

Page 12, line 24: "Simply changing the snow fraction does not improve the agreement. . ." I am not so sure. Increasing the snow fraction will lift the RTM irradiances for shorter wavelengths more strongly than for the long wavelengths (Fig. 4).

R: In principle, this is correct. However, from what we saw in Fig. 12, we currently have a low bias in the surface albedo at short wavelengths, and a high bias at long wavelengths (see Fig. 12). Therefore, simply changing (increasing/decreasing) the snow fraction will not improve the agreement for both long and short wavelengths. We added more explanation in the revised manuscript to avoid confusion (see **Line 3, Page 14**).

Page 13, line 31: "Undetected thin clouds (COT<0.5) led to a high bias. . .." I don't think this statement is justified. Looking at Fig. 8 the measured downward irradiances vary around 200 W m^{-2} and COT vary around 6 (where detected) with consistent RTM results. I assume a COT of 0.5 would produce downward irradiances well below the clear ones but also significantly greater than measured. So the measurements are inconsistent with the presence of thin clouds which makes an explanation as given above (page 11, line 11) more likely.

R: Thank you again for these observations/thoughts. Referring to the response given above (the one with the forward camera imagery + MODIS data), the forward camera indicates that there were indeed some translucent areas where one can see the blue sky through the thin clouds. Our conclusions are given above: "From the below-cloud perspective, the gaps (or very thin clouds) are not large or frequent enough permit the direct beam to be transmitted, leading to an irradiance time series that looks fairly smooth. From the satellite perspective, several sub-grid resolution gaps seem to prevent the detection of a cloud at that pixel." (see more detailed response and figures there).

Page 13, line 32: “. . . above clouds . . .” should be “. . .below clouds. . .” See Fig. 8 and page 11, line 13.

R: Thank you for noticing the typo. We corrected “. . . above clouds . . .” to “. . .below clouds. . .” (see **Line 14, Page 15**).

Table 1 and Table 2: Please indicate in the captions place, time and altitude. Specify above or below cloud conditions and the unit of the numbers. Explain what is listed in the last column called “RTM” The precision of the numbers implies an accuracy that is unrealistic. I assume that the numbers in the first three columns agree within experimental uncertainties but that needs to be specified. Please state the average COT, cloud top and bottom heights.

R: As we mentioned that the Table 1 and Table 2 are removed in the revised manuscript and focus the paper on irradiance comparisons. The last column of “RTM” indicated the estimated irradiance/CRE of the radiative transfer calculations with clouds detected and with clouds undetected in the original manuscript. We agreed the numbers implied an unrealistic accuracy. Since we obtained the uncertainty estimates for the measurements and calculations, we updated the numbers with uncertainties in the manuscript. The COT information of 11 September was provided in the original manuscript (**Line 21, Page 11**). The COT information of 13 September was added in the revised manuscript (**Line 3, Page 12**). The cloud top and bottom heights were added in the revised manuscript (**Line 9, Page 9**; also indicated in Fig. 3).

Fig. 1: Specify the maps’ latitude and longitude ranges, e.g. in the caption. A costal line can be vaguely recognized showing that the flight area was west of Banks Island but I assume hardly any reader is familiar with the area.

R: Thank you for the suggestion. We added the longitude and latitude labels in Fig. 1, and also added the information of the location in the caption (see **Page 24**).

Fig. 2: 80.70% implies a precision that is certainly not justified by the method (see comment in text). Indicate the field of view of the circular areas in (a), the flight altitude, time and location. The y-axis label should read “spectral flux density” or better “spectral irradiance” in accordance with the main text.

R: Thank you for pointing out the precision and uncertainty issue. To justify the snow fraction number, we added an uncertainty analysis for the snow fraction. The uncertainty of the snow fraction for this particular image frame was 4%. Thus, we used “81%±4%” for the snow fraction estimated from the camera imagery. The diameter of the field of view was about 380m based on the aircraft ground speed and altitude of 134m. The FOV size information and the flight altitude, time, and location were added in the figure caption (see **Page 25**).

Thank you for your suggestion. We changed the “spectral flux” to “spectral irradiance” in the y-axis label.

Fig. 3: Approximate times and locations should be specified in the caption. The indicated flight levels are confusing here without additional information.

R: Thank you for the suggestion. On 11 September, MERRA-2 data at 21:00 UTC was averaged over the region of [135W, 130.625W, 72.5N, 74N] to represent the atmospheric profiles. On 13 September, aircraft data from a descending leg (19:31 UTC to 19:50 UTC at 133.8W, 74.1N) was used for the atmospheric profiles. The flight level range indicated in the figures are the flight levels of the aircraft data used for irradiance comparison for above-cloud case (refer to Fig. 7) and below-cloud case (refer to Fig. 8). We added the information to clarify in the revised manuscript (see **Page 26**).

Fig. 4: Given the spectral resolutions, the indicated wavelengths are too precise. 640, 1240 and 1630 nm, as stated in the text, are appropriate.

R: Thank you for your suggestion. We revised the wavelengths in the figure legend to 640, 1240, and 1630 nm (see **Page 27**).

Fig. 5: Consider including open ocean albedo and data by Moody et al., 2007 (see comment in text).

R: Thank you for your suggestion. As we discussed in the previous response, the surface albedo we derived for the dark endmember (snow fraction = 0) was mostly for the surface consisting of dark ice. Therefore, we decided not to include open ocean albedo, but we did include the climatological surface albedo used by the MODIS 1621 cloud retrieval over snow.

Fig. 7 and Fig. 8: Indicate the flight altitudes in captions and maybe the cruise speeds so that the size of the cloud gaps can be inferred.

R: Thank you for the suggestion. We added the flight altitude and cruise speed information in the figure captions (see **Page 30 and 31**).

Fig. 13: Please indicate that these are ratios of downwelling irradiances (I assume).

R: Yes, they are ratios of downwelling irradiances. We added clarifications in the figure caption (see **Page 36**). We also changed the name of the figure to Figure A1.

Appendix B, Fig. 13: Were the solar zenith angles during this flight comparable to those during the other flights? The azimuth dependence may change with solar zenith angle for geometrical reasons and because of a varying (wavelength dependent) contribution of direct irradiance.

R: The solar zenith angles during the calibration flight (2014-10-02) and the flight where the azimuth correction was applied (2014-09-11) were comparable. The data collected during calibration flight (2014-10-02) has solar zenith range of [68.24 º, 71.49 º] with an average of 70.20 º. The solar zenith angle range for the above-cloud case (2014-09-11) is [68.46º to 71.89º] with the mean of 68.91º. We added this information to the revised manuscript to clarify (see **Line 20, Page16**)

Appendix C: In order to understand the meaning of the factor d=1501 the images' total pixel dimension should be stated.

R: The pixel dimension is 2592 (width) ×1944 (height). The information was added to the text (**Line 5, Page 7**).

Technical corrections

Page 4, line 13: Introduce “CRE“ as “cloud radiative effects”

R: As we mentioned in the general response, we decided to remove the discussion of cloud radiative effects. Thus we changed to “… the challenges for deriving shortwave irradiance …”(see **Line 11, Page 4**).

Page 9, line 23: “2014-09-13”

R: Thank you for noticing the typo. We corrected to “2014-09-13” (see **Line 15, Page 10**).

Page 11, line 31: Fig. 7?

R: Thank you for noticing the typo. We corrected to Figure 7 (see **Line 5, Page 13**).

Page 11, line 37: Fig. 7?

R: Thank you for noticing the typo. We corrected to Figure 7 (see **Line 14, Page 13**).

Fig. 5: Wet and dry season colours are hard to distinguish. Second citation should be Brandt et al.

R: We moved the wet and dry season albedo from Fig. 5 to Fig. 6 to avoid confusion and corrected the citation to “Brandt et al.” in the legend of Figure 5.

Fig. 7 and Fig. 8: y-axis: broadband irradiance. Typo “MOODIS” in Fig. 8 Fig. 9 and Fig. 10: y-axis: spectral irradiance

R: Thank you for your suggestion and noticing the typo. We changed the y-axis labels from “flux” to “irradiance” for Figure 7, Figure 8, Figure 9, and Figure 10. We corrected the “MOODIS” to “MODIS” .

The Effect of Low-Level Thin Arctic Clouds on Shortwave Irradiance: Evaluation of Estimates from Spaceborne Passive Imagery with Aircraft Observations

Hong Chen[1,2], Sebastian Schmidt[1,2], Michael D. King[2], Galina Wind[3], Anthony Bucholtz[4], Elizabeth A. Reid[4], Michal Segal-Rozenhaimer[5,6,7], William L. Smith[8], Patrick C. Taylor[8], Seiji Kato[8], Peter Pilewskie[1,2]

[1]University of Colorado, Department of Atmospheric and Oceanic Sciences, Boulder, CO, USA
[2]University of Colorado, Laboratory for Atmospheric and Space Physics, Boulder, CO, USA
[3]Science Systems and Applications, Inc., Lanham, MD, USA
[4]Naval Research Lab, Monterey, CA, USA
[5]Bay Area Environmental Research Institute Sonoma, Sonoma, CA, USA
[6]NASA Ames Research Center, Moffett Field, CA, USA
[7] Department of Geophysics, Porter School of the Environment and Earth Sciences, Tel-Aviv University, Israel
[8]NASA Langley Research Center, Climate Science Branch, Hampton, VA, USA

Correspondence to: Sebastian Schmidt (sebastian.schmidt@lasp.colorado.edu)

Abstract. Cloud optical properties such as optical thickness along with surface albedo are important inputs for deriving the shortwave radiative effects of clouds from space-borne remote sensing. Owing to insufficient knowledge about the snow or ice surface in the Arctic, cloud detection and the retrieval products derived from passive remote sensing, such as from the Moderate Resolution Imaging Spectroradiometer (MODIS), are difficult to obtain with adequate accuracy – especially for low-level thin clouds, which are ubiquitous in the Arctic. This study aims at evaluating the spectral and broadband irradiance calculated from MODIS-derived cloud properties in the Arctic using aircraft measurements collected during the Arctic Radiation-IceBridge Sea and Ice Experiment (ARISE), specifically using the upwelling and downwelling shortwave spectral and broadband irradiance measured by the Solar Spectral Flux Radiometer (SSFR) and the BroadBand Radiometer system (BBR). This starts with the derivation of surface albedo from SSFR/BBR, accounting for the heterogeneous surface in the marginal ice zone (MIZ) with aircraft camera imagery, followed by subsequent inter-comparisons of irradiance measurements and radiative transfer calculations in the presence of thin clouds. It ends with an attribution of any biases we found to causes, based on the spectral dependence and the variations of the measured and calculated irradiance along the flight track.

The spectral surface albedo derived from the airborne radiometers is consistent with prior ground-based and airborne measurements, and adequately represents the surface variability for the study region and time period. Somewhat surprisingly, the primary error in MODIS-derived irradiance fields for this study stems from undetected clouds, rather than from the retrieved cloud properties. In our case study, about 27% of clouds remained undetected, which is attributable to clouds with an optical thickness of less than 0.5. The radiative effect of those clouds that were detected was -40 Wm^{-2} (-39 Wm^{-2}) above (below) the cloud layer, and the optical thickness from the MODIS “1621” cloud product was consistent with the reflected and transmitted irradiance observations.

We conclude that passive imagery has the potential to accurately predict shortwave irradiances in the region if the detection of thin clouds is improved. Of at least equal importance, however, is the need for an operational imagery-based surface albedo product for the polar regions that adequately captures its temporal, spatial, and spectral variability to estimate cloud radiative effects from space-borne remote sensing.

1 Introduction

Understanding the warming of the Arctic necessitates an understanding of the radiative impact of clouds and surface albedo, especially at the surface where the interaction with the cryosphere occurs (Curry et al., 1996; Shupe and Intrieri, 2004). Clouds cool the surface in the shortwave (SW) wavelength range by reflecting solar radiation and warm the surface in the longwave (LW). Low-level, liquid-bearing clouds have recently received special attention because they significantly contributed to the 2012 enhanced Greenland ice melt (Bennartz et al., 2013). When they are optically thin (LWP smaller than 20 gm^{-2}), their SW cooling effect is small because they do not reflect much sunlight, especially when the surface is already bright. In the LW, on the other hand, their emissivity increases rapidly with the liquid water path (LWP), making them blackbodies and warm the surface especially if they are at a low altitude. For larger LWP, the SW cooling eventually dominates as the cloud becomes more reflective.

Valuable data on Arctic clouds has been collected by ground-based observations over the past few decades (Curry et al., 1996, Shupe et al., 2011), but they are limited in spatial coverage and needed to be augmented by additional observations, especially from space-borne remote sensing measurements to help gain meaningful insights of cloud radiative effects in the Arctic as a whole.

Hartmann and Ceppi (2014) used the dataset from the Clouds and the Earth's Radiant Energy System (CERES) and showed that every 10^6 km^2 decrease in September sea ice extent is associated with a 2.5 Wm^{-2} increase in annual-mean absorbed solar radiation averaged over the region from 75º N to 90º N. Kay and L'Ecuyer (2013) used combined products from active and passive remote sensing and showed that during the 2007 summer, the cloud reduction and sea ice loss in the Arctic resulted in more than 20 Wm^{-2} anomalies in shortwave radiation at the top of the atmosphere (TOA). The radiation products used in these studies, e.g., CERES-EBAF (Clouds and Earth's Radiant Energy Systems - Energy Balanced And Filled, Loeb et al., 2012), 2B-FLXHR-LIDAR (Level 2B radiative fluxes and heating rates calculated from radiative transfer model by utilizing radar-lidar cloud and aerosol retrievals from A-Train satellites, Henderson et al., 2013), all rely on coincident cloud observations from the Moderate Resolution Imaging Spectroradiometer (MODIS).

MODIS is a 36-band passive imager onboard the Terra and Aqua satellites. It provides cloud optical parameters (COPs), e.g., cloud optical thickness (COT), cloud effective radius (CER), and cloud thermodynamic phase, from which irradiance can be derived. The COPs from MODIS have been used extensively in studies of cloud radiative effects (e.g., Wielicki et al., 1996; Platnick et al., 2003; Loeb and Manalo-Smith, 2005; Oreopoulos et al., 2016). Due to the lack of temperature and reflectance contrast between clouds and the underlying surface in the Arctic, detecting the clouds is challenging for passive remote sensing, especially when they are thin and occur at a low level. Liu et al. (2010) showed that the MODIS cloud detection algorithm performs better over the ocean than over the ice. The traditional cloud retrieval algorithm (Nakajima and King, 1990) retrieves COT and CER from the reflectance at two channels, one where clouds do not absorb (660, 860, or 1240 nm), and one where cloud drops are weakly absorbing (1630 or 2130 nm). Over snow and ice, the surface albedo is already high in the visible and near-infrared (leaving little dynamic range for cloud remote sensing of optical thickness) and varies regionally and temporally (leading to uncertainties in the retrieval products). This, in combination with low-sun conditions, makes it difficult to obtain accurate cloud optical properties from passive remote sensing. To improve the reliability of MODIS cloud retrievals in the Arctic, an algorithm has been developed that uses two shortwave-infrared bands of 1630 nm and 2130 nm, where snow and ice are relatively dark (Platnick et al., 2001; King et al., 2004). However, the surface albedo varies with surface type even for these bands, and the operational algorithm assumes constant values obtained from a climatology based on 5 years of Terra/MODIS data (Moody et al., 2007).

In addition to the COPs themselves, the snow/ice surface albedo also plays an important role in determining the cloud radiative effect and radiation energy budget in the Arctic (Curry et al., 1995; Shupe and Intrieri, 2004). The surface albedo changes significantly from the visible to the near-infrared wavelength range (Wiscombe and Warren, 1981; Brandt et al., 2005) with different spectral dependence depending on the surface conditions (e.g., snow and ice). Inhomogeneous surface conditions such as floes of partially snow-covered ice, varying snow depth and snow grain size, and surface topography (e.g., sastrugi), all affect the spectral shape and magnitude of the surface albedo. To improve the understanding the inhomogeneous Arctic surface and the spectral dependence of surface albedo, spectral surface albedo measurements for snow and ice have been collected during ground-based field experiments in the polar regions (e.g., Perovich et al., 2002; Brandt et al., 2005). In addition, Perovich et al. (2002) showed that different surface types, e.g., ice, ponds, leads etc., can be identified from aerial camera images through an image processing software. Moreover, a spectral surface albedo model has been developed for different Arctic surfaces such as white sea ice, snow, and melting ponds on sea ice (Malinka et al., 2016 and 2018). However, an operational surface albedo product based on space-borne observations is still not available for the polar regions – in contrast to the land surfaces of the lower latitudes (Strahler et al., 1999).

Finally, accurate knowledge of the water vapor is also important, even in the shortwave (as we will show in this paper). In summary, the challenges for deriving shortwave irradiance from passive remote sensing are (a) inaccurate detection of clouds and cloud optical property retrievals over snow or ice surfaces; (b) lack of accurate surface albedo as a constraint in the radiative transfer model (RTM); (c) insufficient knowledge about the water vapor profile.

The aim of this paper is to use aircraft radiation measurements collected during the NASA Arctic Radiation – IceBridge Sea & Ice Experiment (ARISE, Smith et al., 2017) to evaluate irradiance as derived from coincident satellite imagery, and to investigate the causes of any biases. In the first step, the spectral snow surface albedo was derived from upwelling and downwelling irradiance measurements, accounting for partially snow-covered scenes by the snow fraction estimated from aircraft camera imagery. In the second step, we used an RTM to calculate the upwelling and downwelling broadband and spectral irradiance at flight level, incorporating the MODIS-derived COPs and spectral surface albedo derived from the aircraft measurements as inputs.

The calculated irradiances were then compared with the measured broadband and spectral irradiance pixel by pixel for two cases – above-cloud and below-cloud. Section 2 describes the data and method used in this study. Section 3 provides the results and discussions for the measured spectral surface albedo, as well as for the comparisons between irradiance calculations and measurements. Conclusions are drawn in Section 4.

2 Data and Methods

ARISE was a NASA airborne measurement campaign to study snow and ice properties in the Arctic marginal ice zone (MIZ) in conjunction with cloud microphysics and radiation (Smith et al., 2017). The NASA C-130 aircraft was instrumented with shortwave and longwave radiometers, described in this section, along with cloud microphysics probes, aerosol optical properties instruments, and snow and ice remote sensors. The experiment was based at Eielson Air Force Base near Fairbanks, Alaska, from 2 September to 2 October 2014, to capture the September sea ice minimum. In the Arctic, overpasses of polar-orbiting satellites are fairly common. ARISE targeted multiple overpasses of MODIS and CERES on Aqua, Terra, or VIIRS on Suomi NPP on almost every flight. One of the primary objectives of ARISE was to validate irradiance (or flux densities) derived from CERES-MODIS observations with aircraft radiation measurements. Figure 1 shows two science flights on 11 September and 13 September that sampled above- and below-cloud conditions, respectively. These flights include so-called “lawnmower” patterns, a series of parallel flight legs laterally offset by about 20 km. They were specifically designed for ARISE to sample one or two 100 × 100 km^2 grid boxes per flight with a sufficient number of coincident CERES footprints (each with a 20-km diameter at nadir), as to acquire statistically significant above- or below-cloud aircraft measurements for the validation of CERES-MODIS derived irradiance.

Comparing the aggregated data from ARISE directly with the CERES-MODIS flux products within the grid box, e.g., using histograms, is challenging because of the heterogeneity of the scenes in terms of surface albedo, cloud conditions, and changing solar zenith angle. Therefore, in this paper, we instead compare aircraft observations directly (pixel by pixel) with calculations based on MODIS cloud retrievals along the flight track. The comparison of the aggregated data with CERES-MODIS products is done in a separate publication; we do not use CERES in our analysis because its large footprint does not lend itself to a direct comparison with aircraft data in a heterogeneous environment.

The first step is to merge observations of the broadband shortwave irradiance from the BroadBand Radiometer system (BBR, details in Section 2.1) and of the spectral shortwave irradiance from the solar spectral flux radiometer (SSFR, details in Section 2.2). This merged product combines the high radiometric accuracy and high-fidelity angular response from BBR with the spectral resolution from SSFR, and is referred to as "SSFR-BBR" data. From these data, the surface albedo is derived for low-level legs under clear-sky conditions. To account for the heterogeneous surface (dark ice mixed with snow-covered ice), the surface albedo is acquired as a function of snow fraction, which is estimated from images of a downward-looking video camera (Section 2.3; details on the snow-cover dependent surface albedo derivation in Section 3.1). Finally, atmospheric profiles and reanalysis data (Section 2.4) along with MODIS cloud products are used to calculate all-sky spectral and broadband irradiances along the flight track (Section 2.5), for subsequent comparison with the observations in Sections 3.2 and 3.3.

2.1 BroadBand Radiometer System (BBR)

The BBRs deployed during ARISE are modified CM 22 Precision Pyranometers from Kipp & Zonen (Bucholtz et al., 2010). The BBR included downward-looking and upward-looking sensors. The radiometers were fix-mounted on the aircraft and measured upwelling and downwelling broadband irradiance (unit: W m^{-2}), that is, the spectrally integrated irradiance from 200 nm to 3600 nm. To account for the change of sun-sensor geometry due to aircraft attitude (pitch and roll), a software attitude correction (Long et al., 2010) was applied to the BBR data. In addition, a sunshine pyranometer (SPN-1) was flown to measure diffuse and global radiative fluxes (Badosa et al., 2014; Long et al., 2010). The SPN-1 radiometer was originally intended for ground-based use, but is suited for airborne measurements of global and diffuse radiative fluxes because it does not have any moving parts, unlike traditional instruments such as the Multifilter Rotating Shadowband Radiometer (MFRSR). Smith et al. (2017) provide mission-specific details on both instruments. The BBR has a reported uncertainty of 3% (Smith et al., 2017).

2.2 Solar Spectral Flux Radiometer (SSFR)

To attribute discrepancies between satellite-derived irradiance and airborne observations to causes such as erroneous water vapor, cloud properties, or three-dimensional radiative transfer effects, spectrally resolved measurements are needed (Schmidt and Pilewskie, 2012). SSFR is a moderate resolution flux spectrometer built at the Laboratory for Atmospheric and Space Physics (LASP, University of Colorado Boulder). It is an updated version of the heritage spectrometer system originally developed at NASA Ames (Pilewskie et al., 2003). The SSFR radiometer system consists of two spectrometers for each viewing direction (zenith and nadir): 1) a Zeiss grating spectrometer with a Silicon linear photodiode detector array covering a wavelength range from 350 nm to 950 nm and 2) a Zeiss grating spectrometer with an InGaAs linear photodiode detector array covering a wavelength range from 950 nm to 2150 nm. The spectral resolution of the Silicon channels is 6 nm with a sampling of 4 nm. For the InGaAs channels, the spectral resolution is coarser – 12 nm with 6 nm sampling. From the SSFR measurements, spectral albedo, net flux, and absorption can be derived.

SSFR is typically flown in conjunction with an Active Leveling Platform (ALP, also built at LASP), which was developed for counteracting the changing aircraft attitude to keep the zenith light collector horizontally aligned (the nadir light collector was fix mounted). This is particularly important in the Arctic, where low sun elevations lead to large systematic errors for fix-mounted or poorly stabilized sensors (Wendisch et al., 2001). One reason is that radiation from the lower hemisphere (for example, from clouds below or at the aircraft altitude) is registered by the zenith detector when it is tilted, which leads to systematic biases that cannot be corrected. Another reason lies in the specific design of the SSFR light collectors, which are realized as integrating spheres with a circular aperture on top. They diffuse the incoming light collected by the aperture and bundle it into a fiber optics cable that transmits it to the radiometer system inside the aircraft (Schmidt and Pilewskie, 2012). The integrating sphere has an imperfect response to the incidence (polar) angle θ (Kindel, 2010), in contrast to the response of broadband radiometers such as BBR, which are closer to cos(θ) as required for irradiance. At high sun elevations, a so-called hot spot arises from a baffle that prevents light from being directly transmitted into the fiber optics. Since the response deviates significantly from cos(θ), the direct and the diffuse light need to be corrected. This is done by separating the diffuse and direct component, using radiative transfer calculations in conjunction with SPN-1 measurements (details are provided in Appendix A), and further assuming that the downwelling diffuse radiation is close to isotropic. This assumption is an approximation, which becomes invalid if parts of the lower hemisphere are in the light collector's field of view.

The light collector's angular response to the azimuthal angle also needs to be considered. Throughout the course of the mission, the zenith data revealed a dependence on the relative azimuth of the sun to the aircraft. This dependence was characterized at the end of the mission, by two calibration circles flown on 2 October. The non-homogeneous azimuthal response of the zenith light collector occurred for solar zenith angles greater than 66°. Generally, an azimuthally variable response could either be attributed to aircraft interference (e.g., by the tail and/or propellers of the host aircraft), or to the light collector itself. For the former, BBR and SPN-1 (both fix-mounted on the C-130) would also be affected. To assess their azimuthal response, the attitude-corrected BBR data (Bannehr and Schwiesow, 1993; Bucholtz et al., 2008; Long et al., 2010) was compared with the SPN-1 global irradiance data, as well as with radiative transfer calculations. This comparison revealed that in this case, aircraft interferences were minor compared to atmospheric effects (e.g., cirrus), and that only SSFR measurements, but not BBR and SPN-1, had a significant azimuthal dependence, suggesting the SSFR light collector as the source, rather than aircraft interferences. In order to determine the azimuthal dependence, the SSFR measurements were referenced to the BBR measurement[1] during the calibration circle (details in Appendix B). This azimuthal correction function (dependent on the relative azimuth angle of the aircraft and the sun) was then used for the zenith SSFR data for all research flights. After azimuthal correction, the SSFR downwelling irradiance was scaled to BBR using the method described in Appendix D. It is in this sense that the BBR and SSFR measurements are merged. By using BBR, SPN-1, and SSFR in such a way, the redundancies between the instruments were used to capitalize on the strengths of the individual instruments (BBR: un-biased angular response and high radiometric accuracy; SPN-1: diffuse/global separation; SSFR; spectral resolution for sub-range of BBR and SPN-1). The SSFR nadir signal was also referenced to the BBR data in a similar manner (see Appendix D) because BBR has the better angular response, whereas SSFR provides spectral resolution. The details about the merging method and the uncertainties of the merged irradiance product are provided in Appendix D.

The angular dependence of SSFR was verified in the laboratory. In addition, wavelength and radiometric calibrations were performed before and after the mission. The wavelength calibrations ensured spectral accuracy by referencing the SSFR measurements to several line sources. The primary radiometric calibration, performed with a NIST-traceable calibrated lamp, links SSFR measured digital counts to spectral irradiance. The radiometric calibration was also transferred to a so-called secondary radiometric field standard, which monitored the stability of the radiometers throughout the mission.

---

[1] Since BBR has a near-ideal angular response, the attitude correction with respect to the polar angle can be performed by software as long as data are limited to small deviations from level. By contrast, SSFR with its non-ideal angular response requires an active leveling platform.

2.3 Imagery from Downward-Looking Video Camera

A downward-looking video camera (referred to as "nadir camera") is often included as a standard payload on NASA aircraft. It is a standard, commercially available video camera and typically records scenes for context only and is not radiometrically or geometrically calibrated. Despite this shortcoming, the videos recorded by the nadir camera are used for quantitative image analysis. From the video, we first extract image frames with an average rate of 2 Hz (2 frames per second). The extracted image has a pixel resolution of 2592 (width) ×1944 (height). To co-register the aircraft nadir imagery with the measurements from other instruments, the times for the individual image frames are needed, but the image frames themselves did not contain a digitally stored time. They include a timestamp located at the lower left side that contains time information, and we used Optical Character Recognition (OCR) to retrieve the time from this information.

In the second step, the nadir camera imagery was used to quantify the fractional snow coverage. The snow fraction, which is the fraction of bright pixels of the image, was estimated. To this end, the image was converted from RGB (red, green, and blue) into grayscale by

$$Gray = 0.299R + 0.587G + 0.114B \qquad (1)$$

for each pixel. The weights come from standardized encoding recommendations for television (referred to as BT.601[2]). Another choice would have been to use a single-color channel, or even use the color information to distinguish surface types, but that was not necessary here. For more sophisticated imagery analysis, see Perovich et al. (2002).

One issue of the nadir camera imagery was the darkening effect from the center to the edge of its field of view, which is known as the vignette effect. To compensate, the brightness of the image was linearly increased from edge to center through an image blending and interpolation technique by Haeberli and Voorhies (1994):

$$out = (1 - \beta) \times Black + \beta \times Gray \qquad (2)$$

where *Black* is a black image with the same dimensions as Gray, and β is the image blending factor, a 2D matrix with increasing values of 1.1-1.5 from the image center to the edge. The operator "×" denotes element-by-element multiplication. To avoid the vignetting extremes in the corners, only the imagery within a concentric sampling area was used to derive snow fraction (left panel of Fig. 2a). The key step of the snow fraction detection algorithm is the separation of dark versus bright pixels. To do this, an adaptive thresholding technique was applied. It is an approach for handling an image with unevenly distributed intensities by dividing the image into subimages and assigning different thresholds for each of the subimages (Gonzalez et al., 2002). The details of the adaptive thresholding are described in Appendix C. The snow fraction is then estimated by

$$Frac = \frac{N_{bright}}{N_{total}} \qquad (3)$$

where N_{bright} is the number of pixels above the variable threshold, and N_{total} is the total number of pixels within the sampling area. The imagery and detection results are illustrated in Fig. 2a, whereas Figure 2b shows the simultaneously measured upwelling and downwelling spectral flux. The uncertainties associated with the estimated snow fraction are discussed in Appendix D.

---

[2] https://www.itu.int/dms_pubrec/itu-r/rec/bt/R-REC-BT.601-7-201103-I!!PDF-E.pdf

2.4 C-130 Thermometer and Hygrometer and Modern-Era Retrospective analysis for Research and Applications version 2 (MERRA-2)

The NASA C-130 aircraft was equipped with a thermometer and a hygrometer to measure air temperature and relative humidity, but it did not carry a dropsonde system. Figure 3b shows the profiles derived from the C-130 during a descending leg from 19:31:14 (altitude: 6.447 km) to 19:50:05 (altitude: 0.258 km) on 13 September, 2014. Due to a malfunction of the hygrometer on 11 September, 2014, no water vapor profile from the C-130 is available on this day. Instead (Figure 3a), we used the temperature and water vapor content profiles from MERRA-2, which is an atmospheric reanalysis dataset from NASA (Bosilovich et. al., 2015). MERRA-2 (M2I3NVASM) provides 3-hourly assimilated 3D meteorological fields (dimensions: 576 in longitude; 361 in latitude; 72 pressure levels from 985 hPa to 0.01 hPa). The comparison of the in-situ profiles and MERRA-2 (Figure 3b) shows good agreement, although the reanalysis does not reproduce the details of the vertical profile. A more systematic comparison of reanalysis and in-situ data from ARISE is done by Rozenhaimer et al. (2018) and is not the focus of this paper. The observations reveal much drier and slightly colder conditions than captured in the subarctic climatology from Anderson et al. (1986), referred to here as AFGL. Nevertheless, we used the climatology above 6.5 km to provide complete temperature and water vapor profiles from 0 to 120 km, after rescaling them to the observed temperature and water vapor values at 6.5 km. The constructed atmospheric profiles were then used in the RTM (described in the next subsection) to obtain irradiance calculations.

2.5 Radiative Transfer Calculations based on MODIS Cloud Products

The publicly available pixel-level MODIS cloud products (MOD/MYD06, collection 6.1), which are provided in 5-minute granules (Platnick et al., 2017), are used in this study. The MODIS cloud product includes COPs such as COT, CER, and cloud thermodynamic phase, which are essential parameters for calculating cloud radiative effects. As described before, the MODIS COT and CER are retrieved simultaneously using a bi-spectral reflectance method (Nakajima and King, 1990). To minimize the influence of the surface on cloud retrievals, the 1630 nm and 2130 nm bands are used since the snow and ice surface are relatively dark at those two bands (Platnick et al., 2001; King et al., 2004). These retrievals are included in the MOD/MYD06 files and will be referred to as the “1621” cloud product. Limited in-situ observations suggested that the clouds consisted primarily of liquid water, and the MODIS cloud phase product showed less than 2% of ice clouds along the flight track. Therefore, the clouds were assumed to be liquid.

The MODIS “1621” product includes COPs for cloudy and partially cloudy conditions. The latter are denoted as “PCL” in the MODIS data variable name. The product was extracted along the flight track and then input into a radiative transfer model (RTM) to calculate spectral and broadband irradiance at flight level. A 1-D RTM (libRadtran version 2.0.1, Emde et al., 2016) was used for the calculations. It requires the following inputs:

1) Day of the year (for accurate Sun-Earth distance);
2) Atmospheric profile; here, the subarctic summer atmospheric profile from Anderson et al. (1986) along with:
    a) Water vapor content profile from MERRA-2 for 11 September and from the C-130 hygrometer for 13 September, 2014;
    b) Temperature profile from MERRA-2 for 11 September and from the C-130 thermometer for 13 September, 2014;
3) Solar zenith angle;
4) Wavelength;
5) Surface albedo at the specified wavelength (see Section 3.1);

6) Slit functions (also known as instrument line shape), which describe the bandpass function of the spectrometer. Here, SSFR slit functions as measured in the laboratory are used (full width at half maximum (FWHM) of 6 nm for the Silicon channels and FWHM of 12 nm for InGaAs channels);
7) Cloud optical thickness, and cloud effective radius; here, from MODIS-COPs;
8) Phase functions; here, from Mie calculations distributed with libRadtran;
9) Output altitude grid; here: only at the aircraft flight level.

The RTM uses a solar spectrum with 1 nm resolution as solar source at TOA (Kurucz, 1992). The Discrete Ordinates Radiative Transfer Program (DISORT, Stamnes et al, 1988) is used as the radiative transfer solver. LOWTRAN 7 (Pierluissi and Peng, 1985) is used for the molecular absorption parameterization. The cloud layer altitude was set to 0.8 km to 1.0 km for 13 September according to the water vapor profile from the aircraft hygrometer. Since the hygrometer data was not available for 11 September and the cloud layer could not be identified from the temperature profile, the mean of cloud top height from MODIS and a cloud geometrical thickness of 0.2 km were used in the calculations. The RTM output includes downwelling (global and direct) and upwelling irradiance at the specified wavelengths and output altitude (in this case, at the flight altitude). The cloud layer location and flight level altitude range were indicated in Fig. 3. The wavelength range of the calculations is set to 200 to 3600 nm, which encompasses both BBR and SSFR.

3. Analysis and Results

This section shows the results for the spectral surface albedo derivation from the irradiance data and the aircraft camera imagery, as well as the comparison of broadband and spectral irradiance between aircraft measurements and radiative transfer calculations. The spectral mixed-scene surface albedo parametrization (described first) is used as input to the RTM calculations in the subsequent comparisons with broadband and spectral irradiance observations. Finally, any biases are attributed to different sources based on their spectral fingerprint.

3.1 Spectral Surface Albedo

From the simultaneous measurements of spectral downwelling and upwelling irradiances ($F(\lambda)^{\downarrow}$ and $F(\lambda)^{\uparrow}$), the surface albedo

$$\alpha(\lambda) = \frac{F(\lambda)^{\uparrow}}{F(\lambda)^{\downarrow}} \qquad (4)$$

can be derived through atmospheric correction (Appendix E) from low near-surface legs under clear-sky conditions. Clear-sky measurements were a rare occurrence because low-level clouds were ubiquitous. In this study, we used clear-sky measurements of SSFR-BBR from 20:00:26 UTC to 20:10:51 UTC on 13 September (referred to as “0913-clear-sky”). A time-synchronized video of the flight is provided as supplementary material (S1 “s1_flight-video_20140913-clear-sky.mp4”). This video shows that the Arctic surface varied significantly – from snow scenes to scenes with a large amount of dark ice. Clear-sky scenes (no clouds above or below) were identified from the forward and nadir cameras. During the “0913-clear-sky” case, the aircraft flew at an altitude at around 240 m.

To make full use of the direct measurements of the spectral surface albedo from SSFR-BBR, we parameterized the surface albedo by snow fraction, which can be estimated from the nadir camera imagery (described in Section 2.3). The parameterization was done through a data aggregation technique that combines collective measurements in a partially snow-covered environment. Figure 4 shows the surface albedo at 640 nm, 1240 nm, and 1630 nm plotted versus the snow fraction. The uncertainties of the surface albedo and snow fraction are indicated as vertical and horizontal error bars, respectively (details are provided in Appendix D). The data showed that linear regression can be used to establish a simple relationship between snow fraction and albedo, assuming that each observed spectrum is a mixture of only two so-called end-members: the spectral albedos of a dark and a bright surface. These end-members can vary depending on the local conditions. For example, the dark component can either be open ocean or young ice. The bright component can either be thick ice or a snow-covered surface. The resulting spectral surface albedo for a mixed sampling region is established through the slopes s_λ and intercepts i_λ of the linear fit, with the snow fraction SF ranging from 0 to 1 as the independent variable:

$$\alpha_\lambda = i_\lambda + s_\lambda\, SF \tag{5}$$

The linear regression coefficients (i_λ and s_λ) and associated uncertainties were obtained through orthogonal distance regression (Boggs and Rogers, 1990) for all the SSFR wavelengths except for the water absorption bands, and those less than 350 nm or greater than 1800 nm because of a low signal-to-noise ratio. We provided the coefficients as a supplementary material (see S2 "s2_surface-albedo-coefficients.h5"). This simple surface albedo parameterization has obvious drawbacks; for example, the implicit linear-mixing assumption, the variability of the end-members, and data sparsity of the individual end members (in the example in Fig. 4, snow fractions below 0.6 rarely occur).

The snow spectral end-member (snow fraction of 1) of the mixed-scene spectral surface albedo (referred to as "2014-09-13 surface albedo") is shown in Fig. 5. The error bars of the surface albedo are larger in shortwave than in the near-infrared. As expected, the surface albedo is high in the shortwave range from 400 to 900 nm and decreases in the near-infrared. The SSFR-BBR derived albedo spectra resemble the ground-based measurements of thick snow over ice near Davis Station, Antarctica (Brandt et al., 2005), and they are also close to spring-time aircraft measurements near Barrow (Alaska, Lyapustin et al., 2010). Figure 5 also shows the surface albedo with zero snow fraction. As pointed out above, snow fractions below 0.6 were extremely rare during "0913-clear-sky". Nevertheless, the mixed-surface data, extrapolated to 0 snow fraction, compares surprisingly well to ground-based measurements of young gray ice, taken during the Australian National Antarctic Research Expeditions (ANARE) in 1996 (Warren et al., 1997). The spectra shape of the surface albedo at 0 snow fraction (along with the nadir camera imagery from S1) suggests that during the sampled time period, the dark pixels were ice at various freezing states instead of open ocean. As mentioned above, the binary representation of surface types oversimplifies the actual mixture of ice and snow, but is adequate to serve as surface albedo input for the RTM to constrain the irradiance calculations over mixed surfaces, which is our primary goal here.

3.2 Broadband Irradiance Comparison

In this section, we show broadband irradiance comparisons between SSFR and BBR measurements and MODIS-COPs based RTM calculations at aircraft flight level for an above-cloud case (referred to as "0911-above-cloud") and a below-cloud case (referred to as "0913-below-cloud"), collected by the research flights on 11 September and 13 September, respectively.

The RTM irradiances were calculated for wavelengths from 200 nm to 3600 nm. Since the SSFR-BBR derived surface albedo described in previous subsection was not available at wavelengths shorter than 350 nm, in gas absorption bands, and for wavelengths greater than 1800 nm due to a low signal-to-noise ratio, several techniques were applied to fill in the surface albedo spectra (details in Appendix F). For both the "0911-above-cloud" and "0913-below-cloud" cases, the surface albedo along the flight track was calculated from *SF* as driving parameter to Equation (5). For "0913-below-cloud", *SF* was determined from the camera imagery; for "0911-above-cloud", that was not possible because the surface was not visible through the clouds, and *SF* was instead set to a constant value of 76.4%. This value was obtained by modifying *SF* in Equation (5) to obtain a set of spectral surface albedo that brings the upwelling irradiance calculations at 1640 nm in agreement with the observations for the clear-sky baseline of this case[3]. It should be noted that the observed albedo is the blue-sky albedo (direct beam and diffuse light conditions), whereas the albedo required for the cloud cases is the white-sky albedo (diffuse light only). The difference between the two is discussed by Gardner and Sharp (2010). In addition, it is assumed that the simple parameterization as expressed in Equation (5) holds for the whole study region. This is justified because the measurements occurred in the same general area. Figure 6 shows the surface albedo calculated for *SF*=76.4% for "0911-above-cloud". Comparing with dry- and wet-season surface albedo climatology from Kay and L'Ecuyer (2013), the wet-season climatology agrees well with SSFR-BBR derived surface albedo in the shortwave (wavelength less than 900 nm) except for wavelength 660 nm, where climatology has a higher surface albedo. In the shortwave near-infrared (wavelength greater than 900 nm) however, the dry-season climatology agrees better with SSFR-BBR derived albedo than wet-season. It is worth noting that the surface albedo assumed in MODIS 1621 cloud retrievals (Platnick et al., 2018) agrees with the surface albedo we obtained from SSFR-BBR.

Figure 7 and Fig. 8 show the broadband irradiances from SSFR-BBR, BBR, and the calculations (Fig. 7a: downwelling; Fig. 7b: upwelling) for the "0911-above-cloud", where the aircraft was flying at an altitude around 7 km. The observed variability in the downwelling signal is due to the occurrence of cirrus above the aircraft, which is confirmed by the forward camera. The cirrus was not considered in the RTM because we did not have optical thickness information from MODIS (which does not distinguish between cirrus and low-level clouds) and because we did not pursue radiative closure study as primary purpose of this paper. For the upwelling irradiance, the MODIS-derived baseline value of 230 $\mathrm{Wm^{-2}}$ corresponds to locations where MODIS did not detect any clouds. It is important to note that the value of the baseline indicates the RTM calculations under clear-sky condition, which would change if a different surface albedo parameterization or a different snow fraction were used. For a *SF*=76.4%, the calculations agree with the measurements within 10%. The cloud optical thickness along the flight track (included in Fig 7b) ranges from 0.5 to 15.3, with a median of 5.7, suggesting that MODIS does not retrieve clouds with an optical thickness below 0.5. In contrast to the calculations, the measurements show a continuous variation from leg to leg, suggesting that the clouds actually extended beyond the locations where MODIS detected them. Since the SSFR/BBR sensors integrate the cosine-weighted radiances hemispherically, they do not the same field of view (FOV) as MODIS pixels. The clouds detected by SSFR/BBR but not by MODIS could therefore be caused by clouds located outside the FOV of MODIS. To take this into account, we assume a 45° FOV for the SSFR/BBR that encompasses roughly half of the irradiance signal for an isotropic radiance distribution. When the aircraft was flying at 7 km, the FOV diameter of SSFR/BBR is 7 km (indicated as horizontal bars in Figure 7b, translated into a time range using the aircraft speed). This is larger than the 1 km MODIS pixel-level product FOV. However, the results indicate that cloud portion missed by MODIS exceeds the FOV of the aircraft radiometer and therefore cannot be explained by the mismatch in the observational geometry. To further corroborate that the MODIS algorithm is indeed missing clouds, a sequence of nadir camera imagery (Fig. 7b i - iv) is considered. At close inspection, the images reveal wave patterns, suggesting the existence of thin clouds in regions where MODIS does not detect any. In this case, undetected, optically thin clouds made up more than one fifth of the points along the flight track. Fig. 7b indicates that these undetected clouds lead to an underestimation of the upwelling irradiance by 30 $\mathrm{Wm^{-2}}$ averaged over these pixels (>10% discrepancy). By contrast, the calculated irradiances for the locations where MODIS does detect clouds are only 10 $\mathrm{Wm^{-2}}$ lower than the measurements (4%), which is only slightly larger than the BBR/SSFR measurement uncertainty and can be explained either by (a) incorrect COPs (optical thickness, effective radius, or thermodynamic phase) and/or (b) inaccurate or variable surface albedo. To quantify the contributions of these effects to the total discrepancy, the spectral information from SSFR is used in the next section.

---

[3] See justification under 3.3 and Figure 9b. The data from 21:12:25 UTC to 21:15:35 UTC was selected as the clear-sky baseline.

After the investigation of the above-cloud case for MODIS-derived irradiance, we turn our attention to the below-cloud case – "0913-below-cloud", which relates to near-surface irradiance. The primary cloud layer consisted of stratocumulus cloud and was located between 0.8 and 1.2 km. The cloud optical thickness (indicated in Fig. 8a) ranges from 4.1 to 8.1, with a median of 5.8. A secondary cloud layer close to the surface, located below the aircraft's minimum flight altitude of 500 ft (approximately 150 m), frequently occurs due to a temperature inversion close to the surface, where leads and cracks in the ice provide the necessary moisture for their formation. These clouds also need to be considered to quantify the radiative surface budget, but they are excluded from the analysis here because the aircraft could not underfly them. As a result, only the data from 22:21:00 to 22:25:48 (minimal occurrence of the secondary cloud layer as indicated by the forward and nadir camera imagery) was selected for comparison. A time-synced video for this flight leg is provided in the supplementary materials (see S3 "s3_flight-video_0913-below-cloud.mp4"). As mentioned before, in contrast to the above-cloud case where the surface albedo was held constant in the RTM, the surface albedo variability on the below-cloud leg was considered here. Figure 8 shows the upwelling and downwelling broadband irradiance comparison between calculations and observations from SSFR-BBR and BBR. When incorporating the "13 September surface albedo" into the RTM, the upwelling irradiance calculations resemble the SSFR-BBR and BBR measurements (Fig. 8b). The calculations agreed well with SSFR-BBR and BBR when clouds were detected except for the time period before 22:22:48 UTC when the aircraft was entering the cloud field. The MODIS granule from Aqua was a snapshot of the cloud scene at 22:10, 10 minutes prior to the beginning of the flight leg. Measurement-model discrepancies for specific pixels can therefore be explained by changes of the cloud field over time. The bimodal behavior that is apparent in the time series (Fig. 8a and 8b) as well as in the histograms (Fig. 8c) stems from time periods with and without clouds in the model input. The observations show no evidence of any cloud gap – hence only one mode appears. The "cloud gaps" apparent in the satellite but not aircraft measurements could be caused by different viewing and sun-sensor geometries between the satellite and aircraft instruments. For example, tall clouds could block the direct sun beam measured by the aircraft radiometer when flying below clouds under low-sun conditions. By evaluating the fields of cloud optical thickness and radiance at 860 nm from MODIS (Figures 8e and 8f) and the supplementary flight video S3, we found that any cloud gaps are not large or frequent enough permit the direct beam to be transmitted. This leads to a smooth irradiance time series in the aircraft measurements. The gaps (circled in Fig. 8e, however infrequent, most likely at sub-grid scale for the 1 km product) do seem to cause gaps satellite retrievals. From the distance of the cloudy/clear modes, one can estimate the pixel-level bias caused by undetected clouds: 45 Wm^{-2} bias for the downwelling and 19 Wm^{-2} bias for the upwelling shortwave irradiance.

3.3 Spectral Irradiance Comparison

Although the model-measurement biases in the broadband irradiances are negligible when clouds were detected, the time series as shown in Fig. 7b do not quite match, especially for the thin parts of the clouds near the edge of a field. To diagnose the cause, we use the spectrally resolved measurements by SSFR-BBR in this section.

For the "0911-above-cloud", Fig. 9 presents the spectral upwelling irradiance comparison at 860nm and 1640nm. To put these results into context, the RTM calculations (using Equation (5) with *SF*=76.4%) were also performed with climatological surface albedos of the Arctic dry and wet seasons (0.85 and 0.75) for 860nm from Kay and L'Ecuyer (2013). As shown in Fig. 9a, the baseline of the clear-sky RTM calculations varied significantly with surface albedo. The clear-sky measurements from 21:12:25-21:15:35 UTC are slightly below the *SF*=76.4% baseline calculation for 860 nm, and above for other times. It is impossible to tell whether the variability at this wavelength stems from surface albedo variability or from undetected clouds. For 1640 nm (Fig. 9b), however, the clear-sky baseline is much more defined and less variable, which is why we determined *SF* based on that wavelength.

Since any inaccuracies in the spectral surface albedo will propagate into model biases for both cloudy and clear-sky conditions, an operational surface albedo retrieval in the Arctic would be highly desirable. In this context, it is important to note that the small broadband model-measurement discrepancy of 8 Wm^{-2} from Fig. 7 is only achieved when the SSFR-BBR derived surface albedo is used in the RTM calculations; when using a climatology instead, it would be larger. In other words, in absence of an operational product, the surface albedo variability dominates the uncertainty in clear- and cloudy sky irradiance calculations.

At 1640 nm (Fig. 9b), there is good model-measurement agreement for the clear-sky baseline and for cloudy pixels that MODIS detects. That is because snow is dark in the shortwave infrared, and because MODIS COPs in the Arctic are primarily based on these wavelengths. Because of the obvious distinction between cloudy and clear pixels in the measurements and calculations, it is possible to estimate the fraction of partially or fully cloudy pixels that are not detected by MODIS. Of all pixels along the flight leg with a MODIS-COD below the detection threshold of 0.5 (i.e., “clear”), 27% (highlighted in green) are actually cloudy where MODIS cloud detection algorithm identified as clear-sky. One interesting finding from the broadband irradiance comparison (Fig. 7b) is that the calculations are low-biased relative to the observations. However, from the spectral comparison (Fig. 9), the calculations have larger/similar values than the SSFR measurements at 860 nm/1640 nm. To reconcile the apparently contradictory results, we use the full spectrum from the calculations and observations at 21:24 UTC on 11 September, when the broadband calculation indicates a 6 Wm^{-2} low bias.

Figures 10a and 10b show the spectral upwelling irradiance from the RTM calculations and from the SSFR-BBR measurements, as well as the difference between RTM and SSFR-BBR. In addition to the RTM calculations with atmospheric profiles from MERRA-2 (referred to as RTM$_{\mathrm{MERRA}}$), we provided the calculations with the atmospheric profile climatology (AFGL subarctic summer, Anderson et al., 1986, referred to as RTM$_{\mathrm{AFGL}}$). The agreement between RTM$_{\mathrm{MERRA}}$ and SSFR-BBR in the water vapor absorption bands indicates that MERRA-2 is sufficient to prescribe the water vapor content in the calculations. The broadband irradiance difference between RTM$_{\mathrm{MERRA}}$ and RTM$_{\mathrm{AFGL}}$ due to water vapor is 13.5 Wm^{-2}. Outside of the gas absorption bands, the calculations agree with the measurements at wavelengths smaller than around 850nm, but are slightly low-biased at near-infrared wavelengths. Spectral discrepancies are caused by the use of inaccurate 1) surface albedo 2) cloud optical parameters, some of which compensate each other in the broadband integral. Such error compensation may lead to an improved model-measurements agreement for the “wrong reasons”; therefore, validation efforts should include spectrally resolved measurements.

So far, the analysis did not reveal whether the observed model-measurement discrepancies are due to biases in the COPs or in the surface albedo. Figures 11-12 are an attempt to disentangle both sources of uncertainty despite the limited number of observations during ARISE. Figure 11 shows the ratio between modeled (labeled “RTM”) and measured (“SSFR-BBR”) upwelling broadband irradiance at flight-level as a function of the retrieved COT for the collection of cloudy pixels from 11 September. At large COT, clouds dominate the upwelling irradiance, whereas the surface dominates in the limit of zero COT (as stated above, the retrieved minimum is 0.5). The ratio of RTM/SSFR-BBR can be used to indicate how biased the surface albedo is in the RTM when COT is approaching to 0 and how biased the cloud optical properties are when the COT approaches large values. The data reveal a functional relationship between *COT* and the RTM/SSFR-BBR ratio. An exponential fitting of

$$r = a - e^{b \cdot COT + c} \qquad (6)$$

is used to parameterize the upwelling irradiance ratio as a function of *COT*. The black curve in Fig. 11 suggests that the surface albedo in the calculations is biased low by about 8%, whereas almost no bias is detectable in the cloud properties (a of ~1.01). Figure 12 shows the spectral fits for the wavelengths between 350 and 1800nm. Two spectra are calculated: the spectrum of the ratio when $COT = 0$ (denoted as $r_0(\lambda)$), corresponding to cloud-free conditions; and the spectrum of ratio at infinite *COT* (denoted as $r_\infty(\lambda)$), corresponding to cloudy conditions. The $r_0(\lambda)$ spectrum (red) is consistently lower than 1.0 at short wavelengths (< 1300 nm) and slightly greater than 1.0 for wavelengths longer than 1500 nm. This suggests that the surface albedo is underestimated for the shorter wavelengths and overestimated for the longer wavelengths. Since changing the snow fraction will only increase or decrease surface albedo for all wavelengths, simply changing the snow fraction does not improve the agreement for both long and short wavelengths. As mentioned before, the albedo we used in the RTM is so called blue-sky albedo, which differs from the white-sky albedo that captured by the measured upwelling irradiance under cloudy condition. However, the spectral shape of the two ratios in Figure 12 does not suggest that this had an impact (one would have expected a molecular scattering signature for the shortest wavelengths). Instead, the discrepancies could be caused by the physical changes of the surface, different sun angles, and/or instrument performance changes. The $r_\infty(\lambda)$ spectrum (blue) oscillates around 1.0 for the shorter wavelengths and is consistently larger than 1.0 for longer wavelengths, which suggest that the retrieved effective radius is slightly biased. Unfortunately, owing to limited sampling time, the below-cloud flight (13 September) leg does not lend itself to any conclusions from a cloud transmittance perspective since it is not the same cloud field as on 11 September. In future flight campaigns, coordinated above- and below-cloud legs will furnish more information on bias analyses than possible from ARISE.

4 Conclusions

In this paper, we used aircraft observations to validate shortwave irradiance derived from satellite passive imagery (MODIS) of low-level cloud fields. This was done with two consecutive flights from the NASA ARISE campaign, which sampled the radiation below and above a cloud field in a similar location of the MIZ. Such validation studies are especially important in the Arctic because observations from the surface are sparse. Despite their limitations, passive imagery products are one of the essential data sources for observationally-based estimates of the surface radiative flux under cloudy conditions, which necessitates a quality assessment of cloud detection and the derivation of cloud optical parameters for a variety of specific cloud and surface types as well as surface angles. In addition, accurate knowledge of the surface albedo and of the water vapor vertical distribution is required to derive the net fluxes at the surface, above the cloud layer, and at the top of atmosphere. The two cases analyzed here only focused on one region with one specific surface and cloud type, but this allowed developing a validation approach that can help answer specific questions such as:

1. What is the reliability of passive imagery cloud detection in the MIZ and over solid snow-covered regions?
2. How much do undetected clouds bias imagery-derived irradiance, especially at the surface?
3. What is the relative magnitude of irradiance errors caused by undetected clouds, biased cloud properties, incorrect surface albedo parameterization, and water vapor?

This paper sheds some light on these questions using the combined measured broadband and spectral irradiance in the study region, but these results are far from representative for the Arctic as a whole. To gain a statistically based understanding, validation data from multiple experiments will have to be combined. By aggregating data from multiple missions, it should be possible to answer more general questions, which a single case study cannot address:

- Do existing cloud climatologies from space-borne passive imagery observations accurately reproduce the frequency of low-level optically thin clouds over different surface types?
- Do existing climatologies of surface albedo capture the spatial and temporal variability sufficiently to keep errors in the derived all-sky irradiance and cloud radiative effects to an acceptable level?

It is unclear what “acceptable” would mean for the second question, but our study showed that the actual surface albedo deviates from commonly used climatologies. Throughout the Arctic, inaccurate knowledge of the surface albedo and its variability will lead to an inaccurate estimation of cloud radiative effects and net surface fluxes, even under clear-sky conditions. This is especially important in the visible part of the spectrum where most of the shortwave energy resides, and where the albedo of different surface types (ice, fresh and old snow) varies significantly. Of course, knowledge of the near-infrared variability of snow and ice albedo (via grain size) is also important because it affects the accuracy of imagery-derived cloud products.

To capture the spatial and spectral variability of the surface, we developed a data aggregation technique that combines collective measurements in a partially snow-covered environment into one spectral surface albedo dataset that is parameterized by snow fraction ("binary" representation of the radiative surface properties). The dataset we obtained agrees with ground-based measurements for the two extremes (called spectral end-members): snow and thin ice. In our case, ice-free open ocean was radiatively insignificant, and the two end-members were sufficient to represent the surface variability. In more complex, more general cases, more end-members will be required.

In assessing the relative magnitude of different errors (question 3 above), we found that undetected clouds have the most significant impact on the imagery-derived irradiance. In the case studied here, MODIS did not detect clouds below a threshold of 0.5 in optical thickness, even when including partially cloud-covered pixels. For the above cloud case, this led to a low bias of about 40 Wm^{-2} for the upwelling shortwave irradiance. The below cloud case was harder to interpret due to the limited data and the lack of knowledge about the irradiances at cloud top. However, the model-measurement comparison indicated a high bias of 45 Wm^{-2} in downwelling shortwave irradiance if clouds are not detected, which again suggested the undetected clouds the dominating error source. Secondary error sources are (a) surface albedo, (b) water vapor content, and (c) cloud optical properties. By using an SSFR-BBR derived surface albedo along with atmospheric profiles from aircraft measurements and MODIS-COPs in the RTM calculations, they agreed with the measured spectral and broadband shortwave irradiance within the range of uncertainties, except in regions where MODIS did not detect clouds. It should be pointed out that in absence of an operational surface albedo product, the surface albedo uncertainty by far dominates the calculated shortwave irradiance error.

While the radiation calculations at TOA can be constrained through the radiation product from satellite observations (e.g., CERES), the radiation calculations at the surface do not have such constraints. The attribution of the individual error contributions was done based on measurements from the SSFR-BBR, by distinguishing the different physical mechanisms based on their spectral dependence. Under some circumstances, the different errors compensate partially in the broadband irradiance.

Generalizing the findings from airborne studies such as these will only be possible by improving satellite remote sensing along the way, which in turn requires airborne observations for the development and validation of a new generation of cloud retrievals in the Arctic. Such retrievals will need to account for surface and cloud variability, and address the issue of undetected thin clouds. A database of spectral albedos, acquired with similar techniques as proposed here, would provide the necessary testbed for developing operational space-based retrievals for surface reflectance as available for the lower latitudes. With lower COT thresholds for cloud detection, spatially and temporally dependent surface albedo, accurate cloud retrievals even for thin clouds, passive remote sensing will significantly improve our current understanding of cloud radiative effects in the Arctic. Finally, it will be important to pursue a similar strategy for the thermal wavelength range.

Appendix

A. Diffuse/direct correction for the polar angle response

The polar angle response ("cosine response") needs to be done separately for the direct and the diffuse downwelling radiation. Therefore, these two components first need to be separated, assuming

$$DR(\lambda) = DR_{clear}(\lambda)\cdot f + DR_{cloud}(\lambda)(1-f)$$

where DR is the diffuse (to total, or global) ratio, *f* is the clear-sky fraction, and *(1–f)* is the fraction of a diffuser (clouds).

We can make the simplification $DR_{cloud}(\lambda) = 1.0$, (i.e., the radiation under clouds does not have a direct component), leading to

$$DR(\lambda) = 1 - f\cdot\left(1 - DR_{clear}(\lambda)\right) \tag{A1}$$

The SPN1 measures the broadband diffuse radio, which we denote as DR_{SPN1}:

$$DR_{SPN1} = \frac{\int_{\lambda_1}^{\lambda_2} DR(\lambda)\cdot F^{\downarrow}(\lambda)d\lambda}{\int_{\lambda_1}^{\lambda_2} F^{\downarrow}(\lambda)d\lambda} \tag{A2}$$

where λ_1 and λ_2 indicate the wavelength range of SPN1, and $F^{\downarrow}(\lambda)$ is the calculated downwelling (global) spectral irradiance from a RTM (we did not use the SSFR measurements because they only encompass a sub-range of SPN-1). Substituting Equation (A1) into (A2), we get

$$DR_{SPN1} = 1 - f\cdot\frac{\int_{\lambda_1}^{\lambda_2} F^{\downarrow}(\lambda)\cdot\left(1-DR_{clear}(\lambda)\right)d\lambda}{\int_{\lambda_1}^{\lambda_2} F^{\downarrow}(\lambda)d\lambda} \tag{A3}$$

We can then determine *f* from

$$f = \frac{(1-DR_{SPN1})\cdot\int_{\lambda_1}^{\lambda_2} F^{\downarrow}_{clear}(\lambda)d\lambda}{\int_{\lambda_1}^{\lambda_2} F^{\downarrow}_{clear}(\lambda)\cdot\left(1-DR_{clear}(\lambda)\right)d\lambda} \tag{A4}$$

and the diffuse/direct ratio can be calculated by using this value of *f* in equation (A1).

B. Azimuth response

The azimuth response of the SSFR zenith light collector was obtained using the data collected during the so-called calibration flight (2014-10-02), where the aircraft flew a circles to collect radiation measurements at different solar azimuth angles. This was done by referencing the SSFR irradiance measurements to the simultaneous BBR data, building on the fact that unlike SSFR, BBR had no discernable azimuthal dependence. The data used to determine the azimuth response had a solar zenith range of [68.24 º, 71.49 º] with an average of 70.20 º, whereas the solar zenith angle range for the above-cloud case (2014-09-11, where the azimuth correction was applied) was [68.46º to 71.89º] with the mean of 68.91º.

Since SSFR only covers part of BBR's bandwidth from 200 to 3600 nm, RTM calculations were used to fill in SSFR spectra beyond its nominal wavelength range of 350 – 2050 nm. Subsequently, the RTM-extended SSFR irradiance was spectrally integrated (referred to as F_{SSFR}). A second-order Fourier series was then applied to fit the azimuthal dependence captured by the ratio F_{SSFR}/F_{BBR}, shown in Fig. A1. It shows this ratio as a function of reference azimuth angle, defined as the azimuth angle of the sun with respect to the light collector, for which 0 degrees is defined as the aircraft flying due North. A second-order Fourier series was applied to fit the azimuthal dependence of F_{SSFR}/F_{BBR}. It constitutes SSFR's azimuthal response at this solar zenith angle, which was then used to correct SSFR's downwelling irradiance for the conditions encountered for the SSFR data collected during other research flights. The azimuth response obtained in Fig. A1 can be expressed as (with coefficients)

$$\frac{F_{SSFR}}{F_{BBR}} = 0.9460 + 0.0647\cdot\cos\left(\frac{\phi}{180}\cdot\pi\right) + 0.0160\cdot\sin\left(\frac{\phi}{180}\cdot\pi\right) - 0.0045\cdot\cos\left(\frac{\phi}{180}\cdot 2\pi\right) - 0.0015\cdot\sin\left(\frac{\phi}{180}\cdot 2\pi\right) \tag{A5}$$

where ϕ is the reference azimuth angle.

C. Adaptive thresholding

The threshold value at each pixel location of the image depends on the neighboring pixel intensities I. For a pixel located at (x, y), the threshold value $T(x, y)$ is calculated through the following steps:

1). A subdomain of size $d \times d$ is selected with (x, y) at the center of the subdomain;

2). The weighted average $C(x, y)$ is calculated for the subdomain using Gaussian weights (Davies 1990) $W(x, y)$, $C(x, y) = \sum_{i=0}^{d} \sum_{j=0}^{d} I(i, j) \cdot W(i, j)$;

3). The threshold for the pixel at (x, y) is the difference of the weighted average calculated in the previous step and a constant C_0, $T(x, y) = C(x, y) - C_0$.

d and C_0 are input parameters that can be adjusted to improve the results. In this study, d is set to 1501 and C_0 is set to 0.

D. Uncertainty estimation

1). SSFR-BBR irradiance product

For the SSFR spectral measurements, the nominal radiometric uncertainty is 5% (Schmidt et al., 2010). The nominal uncertainty of BBR measurements is 3% (Smith et al., 2017). As we described in section 2.2, we corrected the azimuthal dependence of SSFR downwelling irradiance based on the BBR measurements using the method described in Appendix B. After the correction, the SSFR downwelling and upwelling irradiances are still slightly inconsistent with BBR due to an imperfect cosine response comparing to BBR (although they agree with BBR within the range of uncertainty). In addition, the different sun-sensor geometries between the calibration flight (2 October, 2014) and the “0911-above-cloud” case mean that the azimuthal response as measured during the calibration flight does not necessarily fully apply to the case under study. In order to reference SSFR to BBR and simultaneously estimate the uncertainty of the merged product (SSFR-BBR), we applied a scaling method as shown in Fig. A2. Figures A2 (a) and (b) show the azimuthally corrected SSFR downwelling and SSFR upwelling irradiance versus BBR. The wide spread of downwelling irradiance indicates that even after applying azimuthal correction for SSFR, some residual uncertainty of the azimuthal response obtained in Appendix B remains in the SSFR measurements after the azimuthal correction. In the upwelling irradiance, the SSFR is more closely related to BBR. Figures A2 (c) and (d) illustrate how we correct for the remaining biases between SSFR and BBR and estimate the uncertainties of the SSFR-BBR product. Figures A2 (c) and (d) show the histogram of the ratio of SSFR and BBR measurements. The ratio histograms indicate a scale factor of 1.006 and 0.946 for the SSFR downwelling and upwelling, with standard deviations of 0.025 and 0.01 when referencing to BBR. The scale factors of 1.006 and 0.946 are applied as divisor to SSFR downwelling and upwelling irradiance respectively. The SSFR irradiance after scaling (referred to as SSFR-BBR) versus BBR is shown in Figures A2 (a) and (c) in green. After scaling, the SSFR-BBR and BBR achieve a better consistency. The standard deviations of 0.025 and 0.01 represent the precision for the downwelling and upwelling irradiance of SSFR-BBR. Thus, we use 2.5% (0.025/1.006*100%) and 1% (0.01/0.946*100%) as the precision estimates for SSFR-BBR downwelling and upwelling, whereas the uncertainty propagates from BBR into the SSFR-BBR product (3%).

2). Snow fraction and surface albedo

When calculating the surface albedo from SSFR-BBR using Equation (4), we use the precision as determined above because the uncertainty cancels out for the ratio between the upwelling and downwelling irradiance. The uncertainty estimate of 2.7% for the surface albedo α is then obtained through error propagation using Equation (4), where

$$\frac{u(\alpha(\lambda))}{\alpha(\lambda)} = \sqrt{\left(\frac{u(F(\lambda)^{\uparrow})}{F(\lambda)^{\uparrow}}\right)^2 + \left(\frac{u(F(\lambda)^{\downarrow})}{F(\lambda)^{\downarrow}}\right)^2} \qquad \text{(A6)}$$

The uncertainty of the snow fraction described in Section 2.3 is estimated based on two main sources of error:

1. Angle of the field of view (FOV): defined the circular area of the image pixels that were selected for processing;
2. The subdomain size d specified in the adaptive thresholding method described in Appendix C.

When the FOV size mentioned gets too large, pixels affected by the vignette effect and beyond correction is included, which will bias the results. When the FOV size gets too small, we would lose the variation of the snow fraction due to a relative small area. To use as many pixels as possible while avoiding to include contaminated pixels due to vignette effect at the corners, we found the best FOV angle to be 70°. In addition, changing the subdomain size d would slightly change the results. Thus, we obtained 5 sets of snow fraction estimates using FOV angle of 60°, 70°, 80° and a subdomain size d of 1401, 1501, and 1601. Fig. A3 shows the 5 sets of snow fractions estimated from nadir camera images using before-mentioned FOV angles and subdomain sizes. The standard deviation of the 5 sets of snow fraction is used as the uncertainties for the snow fraction for each data point.

3). Radiative transfer calculations

The uncertainty of the radiative transfer (RT) calculations for the “0911-above-cloud” was estimated through the two-stream approximation of the reflectance R

$$R = \frac{\tau + \alpha \cdot (\frac{2\mu}{1-g})}{\tau + (\frac{2\mu}{1-g})} \tag{A6}$$

where τ is the cloud optical thickness, α is the surface albedo, μ is the cosine of the solar zenith angle, and g is the asymmetry parameter. The value of 0.85 is assume for g. In addition, we assume that the two main sources for the uncertainty are from the cloud optical thickness τ and surface albedo α. The uncertainty of R due to the change of τ and α is therefore

$$u(R) = \sqrt{\left(\frac{\partial R}{\partial \tau} u(\tau)\right)^2 + \left(\frac{\partial R}{\partial \alpha} u(\alpha)\right)^2} \tag{A7}$$

This analytical formula allows to calculate uncertainties without numeric radiative transfer calculations.

E. Atmospheric correction

The following steps describe the atmospheric correction applied to the flight level albedo measured by SSFR-BBR.

1) The spectral flight level albedo from SSFR-BBR (referred to as x_0) was scaled by 0.6, 0.7, 0.8, 0.9, and 1.0 (referred to as y_1, y_2, y_3, y_4, and y_5) – each of these are spectra;
2) Five sets of downwelling and upwelling irradiances were obtained from the RTM by changing surface albedo to y_1, y_2, y_3, y_4, and y_5 while keeping the other model inputs the same;
3) From the five sets of downwelling and upwelling irradiances calculated at flight altitude, we can derive five corresponding flight level albedo x_1, x_2, x_3, x_4, and x_5 using Equation (4);
4) The five pairs of $\{x, y\}$ provide a relationship between surface albedo and flight level albedo (nearly linear), $y = ax + b$;
5) The linear relationship was inverted to infer the surface albedo spectrum from the measurements at flight level ($ax_0 + b$).

The atmospheric correction corrected less than 0.2% on flight level albedo at the non-absorbing wavelengths.

F. Extending spectral surface albedo

To obtain the spectral surface albedo for a wavelength range from 200 nm to 3600 nm, several techniques were performed. Using the spectral surface albedo for “0911-above-cloud” (Fig. 6) as an example, the following steps were followed:

1) The spectral surface albedo was calculated from equation (5), e.g., with *SF*=76.4% (marked in red in Fig. 6);
2) In the gas absorption bands (red area in Fig. 6), the surface albedo was replaced with interpolated values;

3) From 1800nm to 1900nm (yellow area in Fig. 6), a polynomial fit was used for extrapolation, based on the spectral dependence from 1650 nm to 1800 nm;
4) For the wavelengths shorter than 350 nm and greater than 1900 nm (green area in Fig. 6), a modeled snow albedo (Wiscombe and Warren, 1981) was used, multiplied with a scale factor to match the measurements at the joinder wavelengths.

Acknowledgements. This work was supported by NASA grants NNX12AC11G (SSFR data collection during ARISE) and NNX14AP72G (data analysis). MODIS data were provided by the NASA/Goddard Space Flight Center's Level-1 and Atmosphere Archive and Distribution System (LAADS) (http://dx.doi.org/10.5067/MODIS/MOD06_L2.061).

References

Anderson, G. P., Clough, S. A., Kneizys, F. X., Chetwynd, J. H., and Shettle, E. P.: AFGL atmospheric constituent profiles (0 - 120km). Tech. Rep. AFGL-TR-86–0110, (954), 46, 1986.

Badosa, J., Wood, J., Blanc, P., Long, C. N., Vuilleumier, L., Demengel, D., and Haeffelin, M.: Solar irradiances measured using SPN1 radiometers: Uncertainties and clues for development, Atmos. Meas. Tech., 7(12), 4267–4283, doi:10.5194/amt-7-4267-2014, 2014.

Bannehr, L., and Schwiesow, R.: A technique to account for the misalignment of pyranometers installed on aircraft, J. Atmos. Ocean. Tech., 10, 774–777, 1993.

Bennartz, R., Shupe, M. D., Turner, D. D., Walden, V. P., Steffen, K., Cox, C. J., Kulie, . S., Miller, N.B., and Pettersen, C.: July 2012 Greenland melt extent enhanced by low-level liquid clouds. Nature, 496, 83–86, 2013.

Boggs, P. T. and Rogers J. E.: Orthogonal distance regression. Contemporary Mathematics, 112, 183-94, 1990.

Bosilovich, M., Akella, S., Coy, L., Cullather, R., Draper, C., Gelaro, R., Kovach, R., Liu, Q., Molod, A., Norris, P., Wargan, K., Chao, W., Reichle, R., Takacs, L., Vikhliaev, Y., Bloom, S., Collow, A., Firth, S., Labow, G., Partyka, G., Pawson, S., Reale, O., Schubert, S. D., and Suarez, M: MERRA-2: Initial evaluation of the climate. NASA Tech. Rep. Series on Global Modeling and Data Assimilation NASA/TM-2015-104606, 2015

Brandt, R. E., Warren, S. G., Worby, A. P., and Grenfell, T. C.: Surface albedo of the Antarctic sea ice zone, J. Climate, 18, 3606–3622, 2005.

Bucholtz, A., Bluth, R. T., Kelly, B., Taylor, S., Batson, K., Sarto, A. W., Tooman, T P., and McCoy, Jr., R. F.: The Stabilized Radiometer Platform (STRAP) - An actively stabilized horizontally level platform for improved aircraft irradiance measurements, J. Atmos. Ocean. Tech, 25, 2161–2175, 2008.

Bucholtz, A., Hlavka, D. L., McGill, M. J., Schmidt, K. S., Pilewskie, P., Davis, S. M., Reid, E. A., and Walker, A. L.: Directly Measured Heating Rates of a Tropical Subvisible Cirrus Cloud, J. of Geophys. Res., 115, 1-11, 2010.

Curry, J. A., Schramm, J. L., Serreze, M. C., and Ebert, E. E.: Water vapor feedback over the Arctic Ocean, J. Geophys. Res., 100, 14223–14229, 1995.

Curry, J. A., Rossow, W. B., Randall, D., and Schramm, J. L.: Overview of arctic cloud and radiation characteristics, J. Climate, 9, 1731–1764, 1996.

Davies, E. R.: Machine Vision: Theory, Algorithms, Practicalities, 3rd Edition, Elsevier, Inc., 934 pp., 2005.

Emde, C., Buras-Schnell, R., Kylling, A., Mayer, B., Gasteiger, J., Hamann, U., Kylling, J., Richter, B., Pause, C., Dowling. T. and Bugliaro, L.: The libRadtran software package for radiative transfer calculations (version 2.0.1), Geosci. Model Develop., 9, 1647–1672, doi:10.5194/gmd-9-1647-2016, 2016.

Gardner, A. S., and Sharp, M. J.: A review of snow and ice albedo and the development of a new physically based broadband albedo parameterization. J. Geophys. Res., 115, F01009, doi:10.1029/2009JF001444, 2010.

Gonzalez, R. C., Woods, R. E., and Eddins, S. L.: Image Segmentation. Digital Image Processing, 600–603, 2002.

Haeberli, P., and Voorhies, D.: Image processing by linear interpolation and extrapolation, IRIS Universe Magazine, 28, 8–9, 1994.

Hartmann, D. L., and Ceppi, P.: Trends in the CERES dataset, 2000-13: The effects of sea ice and jet shifts and comparison to climate models, J. Climate, 27, 2444–2456, 2014.

Henderson, D. S., L'Ecuyer, T., Stephens, G., Partain, P., and Sekiguchi, M.: A multisensor perspective on the radiative impacts of clouds and aerosols, J. Appl. Meteorol. Clim., 52, 853–871, 2013.

Kay, J. E., and L'Ecuyer, T.: Observational constraints on Arctic Ocean clouds and radiative fluxes during the early 21st century, J. Geophys. Res., 118, 7219–7236, 2013.

Kindel, B. C.: Cloud shortwave spectral radiative properties: Airborne hyperspectral measurements and modeling of irradiance, Ph.D. Dissertation, University of Colorado Boulder, United States, 130 pp., 2010.

King, M. D., Platnick, S., Yang, P., Arnold, G. T., Gray, M. A., Riedi, J. C., Ackerman, S. A., and Liou, K. N.: Remote sensing of liquid water and ice cloud optical thickness and effective radius in the Arctic: Application of airborne multispectral MAS data, J. Atmos. Ocean. Tech, 21, 857–875, 2004.

Kurucz, R. L.: Synthetic infrared spectra, In Infrared Solar Physics, Rabin, D. M., Jefferies, J. T., and Lindsey, C. (Eds.), Springer-Science+Business Media, B. V., 523–531, 1992.

Lyapustin, A., Gatebe, C. K., Kahn, R., Brandt, R., Redemann, J., Russell, P., King, M. D., Pedersen, C. A., Gerland, S., Poudyal, R., Marshak, A., Wang, Y., Schaaf, C., Hall, D., and Kokhanovsky, A.: Analysis of snow bidirectional reflectance from ARCTAS Spring-2008 campaign, Atmos. Chem. Phys., 10, 4359–4375, 2010.

Liu, Y., Ackerman, S. A., Maddux, B. C., Key, J. R., and Frey, R. A.: Errors in cloud detection over the arctic using a satellite imager and implications for observing feedback mechanisms, J. Climate, 23, 1894–1907, 2010.

Loeb, N. G., and Manalo-Smith, N.: Top-of-atmosphere direct radiative effect of aerosols over global oceans from merged CERES and MODIS observations, J. Climate, 18, 3506–3526, 2005.

Loeb, N. G., Kato, S., Su, W., Wong, T., Rose, F. G., Doelling, D. R., Norris, J. R., and Huang, X.: Advances in understanding top-of-atmosphere radiation variability from satellite observations, Surv. Geophys., 33, 359–385, 2012.

Long, C. N., Bucholtz, A., Jonsson, H., Schmid, B., Vogelmann, A., and Wood, J.: A method of correcting for tilt from horizontal in downwelling shortwave irradiance measurements on moving platforms, The Open Atmos. Sci. J., 4, 78–87, 2010.

Malinka, A., Zege, E., Heygster, G., and Istomina, L.: Reflective properties of white sea ice and snow, The Cryosphere, 10, 2541–2557, https://doi.org/10.5194/tc-10-2541- 2016, 2016.

Malinka, A., Zege, E., Istomina, L., Heygster, G., Spreen, G., Perovich, D., and Polashenski, C.: Reflective properties of melt ponds on sea ice, The Cryosphere, 12, 1921–1937, https://doi.org/10.5194/tc-12-1921-2018, 2018.

Moody, E. G., King, M. D., Schaaf, C. B., Hall, D. K., and Platnick, S.: Northern Hemisphere five-year average (2000-2004) spectral albedos of surfaces in the presence of snow: Statistics computed from Terra MODIS land products, Remote Sens. Environ., 111, 337–345, 2007.

Nakajima, T., and King, M. D.: Determination of the optical thickness and effective particle radius of clouds from reflected solar radiation measurements. Part I: Theory, J. Atmos. Sci., 47, 1878–1893, 1990.

Oreopoulos, L., Cho, N., Lee, D., and Kato, S.: Radiative effects of global MODIS cloud regimes, J. Geophys. Res., 121, 2299–2317, 2016.

Perovich, D. K., Tucker, W. B., and Ligett, K. A.: Aerial observations of the evolution of ice surface conditions during summer, J. Geophys. Res., 107, SHE24-1–SHE24-14, https://doi.org/10.1029/2000JC000449, 2002.

Perovich, D. K.: Seasonal evolution of the albedo of multiyear Arctic sea ice, J. Geophys. Res., 107(C10), 8044, doi: 10.1029/2000JC000438, 2002.

Pierluissi, J. H., and Peng, G. : New molecular transmission band models for LOWTRAN, Optical Engineering, 24, 541–547, doi: 10.1117/12.7973523, 1985.

Pilewskie, P., Pommier, J., Bergstrom, R., Gore, W., Howard, S., Rabbette, M., Schmid, B., Hobbs, P. V., and Tsay, S. C.: Solar spectral radiative forcing during the Southern African Regional Science Initiative, J. Geophys. Res., 108(D13), 8486, doi:10.1029/2002JD002411, 2003.

Platnick, S., Li, J. Y., King, M. D., Gerber, H., and Hobbs, P. V.: A solar reflectance method for retrieving the optical thickness and droplet size of liquid water clouds over snow and ice surfaces, J. Geophys. Res., 106, 15185–15199, 2001.

Platnick, S., King, M. D., Ackerman, S. A., Menzel, W. P., Baum, B. A., Riédi, J. C., and Frey, R. A.: The MODIS cloud products: Algorithms and examples from Terra, IEEE Trans. Geosci. Remote Sens., 41, 459–473, 2003.

Platnick, S., Ackerman, S. A., King, M. D., Wind, G., Meyer, K., Menzel, W. P., Frey, R. A., Holz, R. E., Baum, B. A., and Yang, P.: MODIS Atmosphere L2 Cloud Product (06_L2). NASA MODIS Adaptive Processing System, Goddard Space Flight Center, USA, http://dx.doi.org/10.5067/MODIS/MOD06_L2.006, 2017.

Platnick, S., Meyer, K. G., King, M. D., Wind, G., Amarasinghe, N., Marchant, B., Arnold, G. T., Zhang, Z., Hubanks, P. A., Holz, R. E., and Yang, P.: The MODIS cloud optical and microphysical products: Collection 6 updates and examples from Terra and Aqua, IEEE Trans. Geosci. Remote Sens., 55, 502-525, 2017.

Platnick, S., Meyer, K. G., King, M. D., Wind, G., Amarasinghe, N., Marchant, B., Arnold, G. T., Zhang, Z., Hubanks, P. A., Ridgway, B., and Riedi, J.: MODIS Cloud Optical Properties: User Guide for the Collection 6/6.1 Level-2 MOD06/MYD06 Product and Associated Level-3 Datasets version 1.1, https://atmosphere-imager.gsfc.nasa.gov/sites/default/files/ModAtmo/MODISCloudOpticalPropertyUserGuideFinal_v1.1.pdf, 2018.

Rozenhaimer, M., Barton, N., Redemann, J., Schmidt, S., LeBlanc, S., Anderson, B., Winstead, E., Corr, C. A., Moore, R., Thornhill, K. L., and Cullather, R. I.: Bias and sensitivity of boundary layer clouds and surface radiative fluxes in MERRA-2 and airborne observations over the Beaufort Sea during the ARISE campaign, J. Geophs. Res. Atmos., 123, doi: 10.1029/2018JD028349.

Schmidt, S., Pilewskie, P., Mayer, B., Wendisch, M., Kindel, B., Platnick, S., King, M. D., Wind, G., Arnold, G. T., Tian, L., Heymsfield, G., and Kalesse, H.: Apparent absorption of solar spectral irradiance in heterogeneous ice clouds, J. Geophys. Res., 115, D00J22, doi:10.1029/2009JD013124, 2010.

Schmidt, S., and Pilewskie, P.: Airborne measurements of spectral shortwave radiation in cloud and aerosol remote sensing and energy budget studies, In A. A. Kokhanovsky (Ed.), Light Scattering Reviews, Vol. 6: Light Scattering and Remote Sensing of Atmosphere and Surface, Berlin, Heidelberg: Springer Berlin Heidelberg, 239–288, doi:10.1007/978-3-642-15531-4_6, 2012.

Shupe, M. D., Walden, V. P., Eloranta, E., Uttal, T., Campbell, J. R., Starkweather, S. M., and Shiobara, M.: Clouds at Arctic atmospheric observatories. Part I: Occurrence and macrophysical properties, J. Appl. Meteorol. Clim., 50, 626–644, 2011.

Shupe, M. D., and Intrieri, J. M.: Cloud radiative forcing of the Arctic surface: The influence of cloud properties, surface albedo, and solar zenith angle, J. Climate, 17, 616–628, 2004.

Smith, W. L., Hansen, C., Bucholtz, A., Anderson, B. E., Beckley, M., Corbett, J. G., Cullather, R. I., Hines, K.M., Hofton, M., Kato, S., Lubin, D., Moore, R. H., Segal Rosenhaimer, M., Redemann, J., Schmidt, S., Scott, R., Song, S., Barrick, J. D., Blair, J.B., Bromwich, D. H., Brooks, C., Chen, G., Cornejo, H., Corr, C. A., Ham, S., Kittelman, A. S., Knappmiller, S., LeBlanc, S., Loeb, N. G., Miller, C., Nguyen, L., Palikonda, R., Rabine, D., Reid, E. A., Richter-Menge, J. A., Pilewskie, P., Shinozuka, Y., Spangenberg, D., Stackhouse, P., Taylor, P., Thornhill, K. L., van Gilst, D., and Winstead, E.: Arctic Radiation-IceBridge Sea and Ice Experiment: The Arctic radiant energy system during the critical seasonal ice transition. Bull. Amer. Meteor. Soc., 98, 1399–1426, https://doi.org/10.1175/BAMS-D-14-00277.1, 2017

Stamnes, K., Tsay, S.-C., Wiscombe, W., and Jayaweera, K.: Numerically stable algorithm for discrete-ordinate-method radiative transfer in multiple scattering and emitting layered media, Appl. Opt., 27, 2502–2509, 1988.

Strahler, A. H., Lucht, W., Schaaf, C. B., Tsang, T., Gao, F., Li, X., Muller, J., Lewis, P., and Barnsley, M. J.: MODIS BRDF/albedo product: algorithm theoretical basis document version 5.0, https://lpdaac.usgs.gov/documents/97/MCD43_ATBD.pdf, 1999.

Warren, S. G., Roesler, C. S., and Brandt, R. E.: Solar radiation processes in the east Antarctic sea-ice zone. Antarctic J. United States, 32, 185–186, 1997.

Wendisch, M., Müller, D., Schell, D., and Heintzenberg, J.: An airborne spectral albedo meter with active horizontal stabilization, J. Atmos. Ocean. Tech, 18, 1856–1866, 2001.

Wielicki, B. A., Barkstrom, B. R., Harrison, E. F., Lee III, R. B., Smith, G. L., and Cooper, J. E.: Clouds and the Earth's Radiant Energy System (CERES): An Earth Observing System Experiment. Bull. Amer. Meteor. Soc., 77, 853–868, 1996.

Wiscombe, W. J., and Warren, S. G.: A model for the spectral albedo of snow. I: Pure snow, J. Atmos. Sci., 37, 2712–2733, 1981.

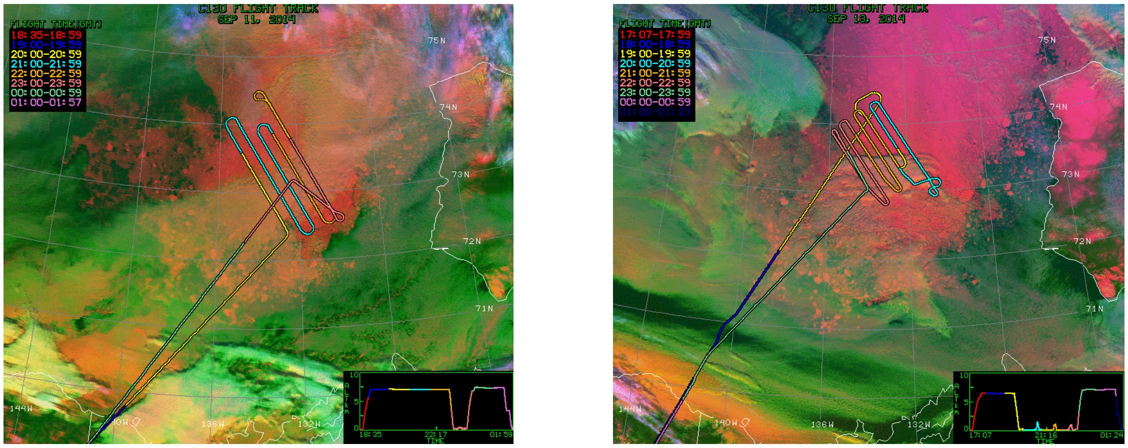

11 September

13 September

Figure 1. ARISE flight tracks overlaid on MODIS false color imagery (0.65 μm for red, 11 μm for blue, and 3.7-11 μm for green) from NASA Langley Research Center on 11 September and 13 September 2014. The focus region if these two research flights was [136W, 130W, 72.5N, 74.5N] in the marginal ice zone.

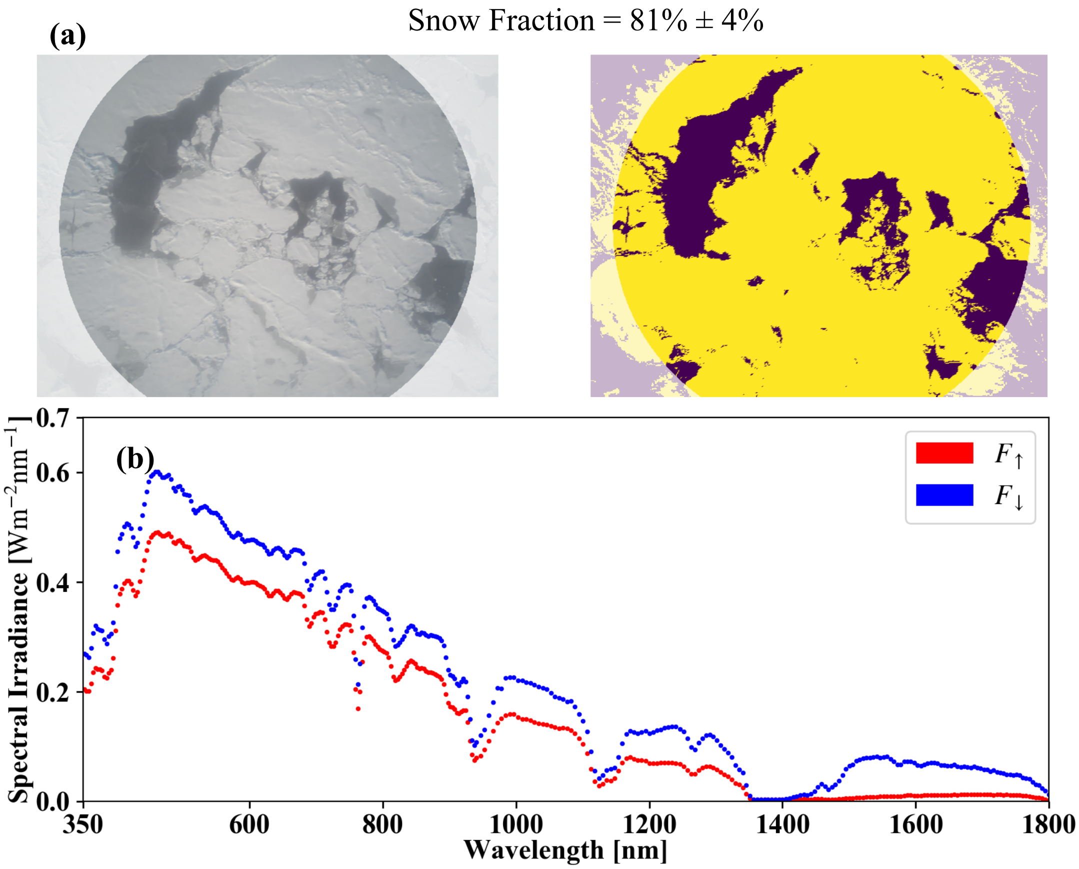

Figure 2. **(a)** An example of the snow fraction along with its uncertainty estimated from the nadir camera imagery at 20:03:32 UTC on 13 September, at a location of (-132.95º, 73.85º). The flight altitude was 134 m. The left panel is the nadir camera imagery. The diameter of the field of view was about 380 m. The right panel uses yellow and purple to indicate bright and dark pixels as detected by the adaptive thresholding method. The snow fraction is derived from the abundance of yellow pixels. **(b)** The upwelling and downwelling irradiance from SSFR-BBR at the same time.

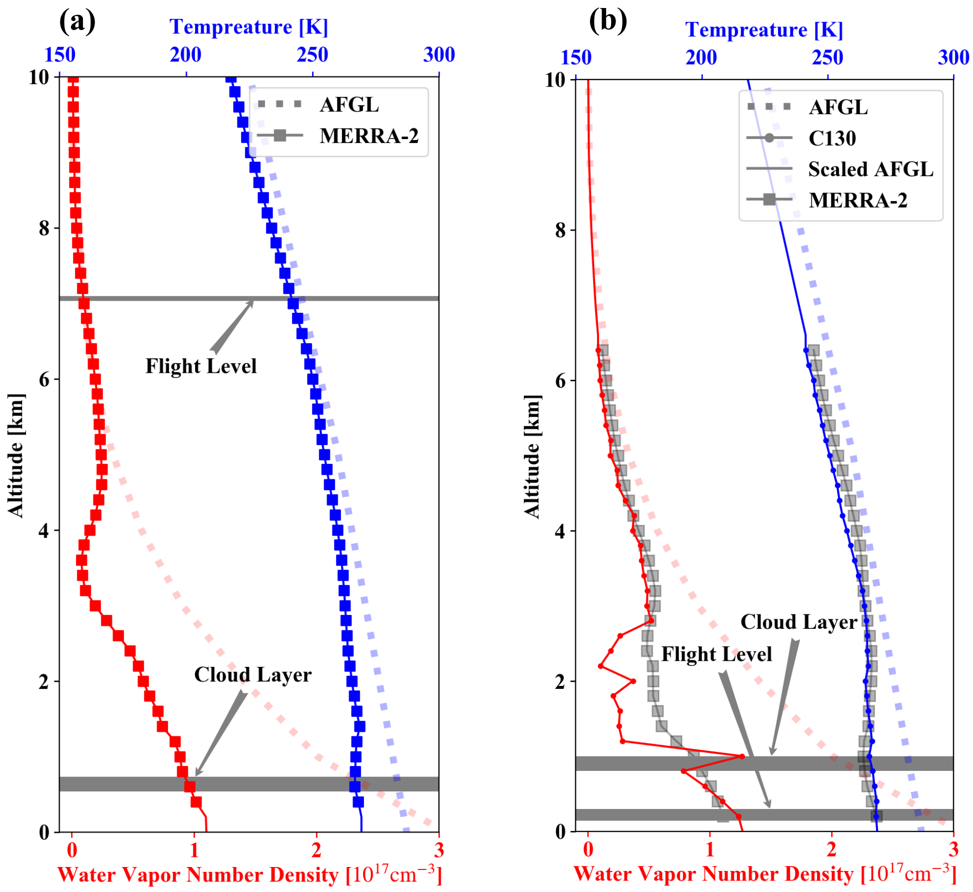

Figure 3. Vertical profiles of temperature and water vapor from MERRA-2 and from the climatology (AFGL) for (a) 11 September and (b) from the C130 for 13 September 2014. On 11 September, MERRA-2 data at 21:00 UTC was averaged over the region of [135W, 130.625W, 72.5N, 74N] to represent the atmospheric profile there. The vertical cloud distribution was unavailable from the in-situ data. On 13 September, aircraft data from a descending leg (19:31 UTC to 19:50 UTC at 133.8W, 74.1N) was used for the atmospheric profiles. Based on the water vapor profile, the cloud was likely located below 1.0 km (indicated in grey). Since hygrometer measurements were not available on 11 September, the cloud top height (1.1 km) was obtained from the MODIS L2 product), and the geometric thickness was set to 0.2 km (just like on September 13). The flight level range is also shown. The solid lines for both days represent the temperature and water vapor profiles that went into the radiative transfer calculations.

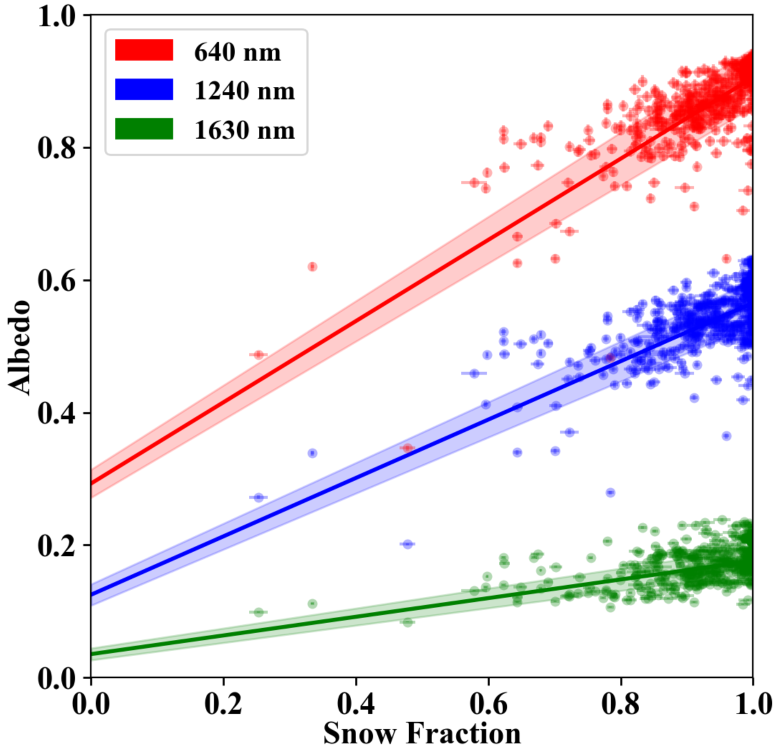

Figure 4. Estimated snow fraction from nadir imagery versus SSFR-BBR measured surface albedo at 640 nm, 1240 nm, and 1630 nm. The surface albedo and snow fraction uncertainties are indicated as vertical and horizontal error bars. The solid lines show linear regression fits, and the shaded region indicates their uncertainties.

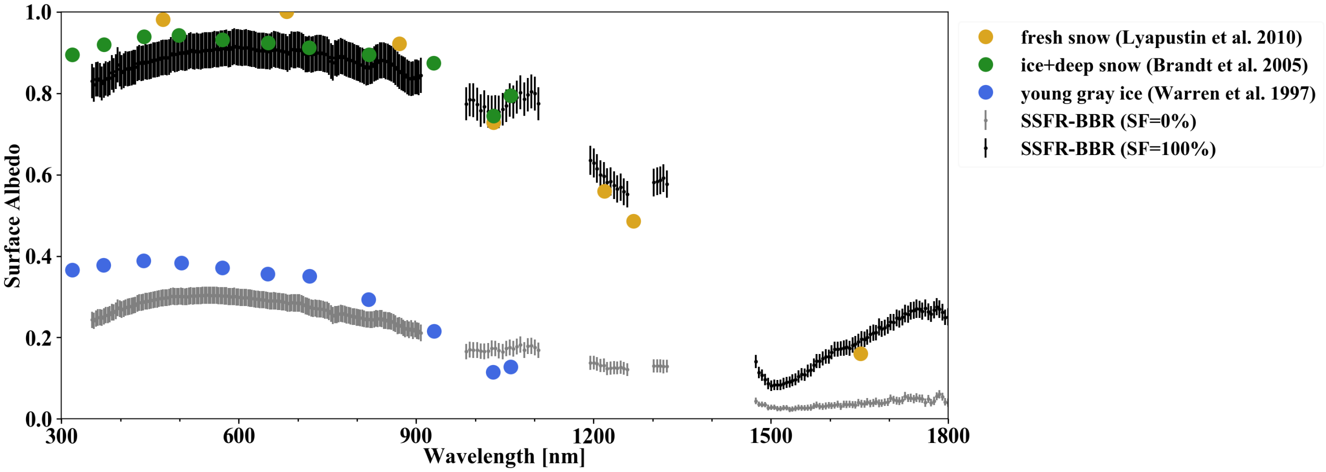

Figure 5: Spectral surface albedo derived from SSFR-BBR measurements for *SF*=100% (black) and *SF*=0 (gray), along with their uncertainties. In addition, different albedos from the literature are shown for comparison.

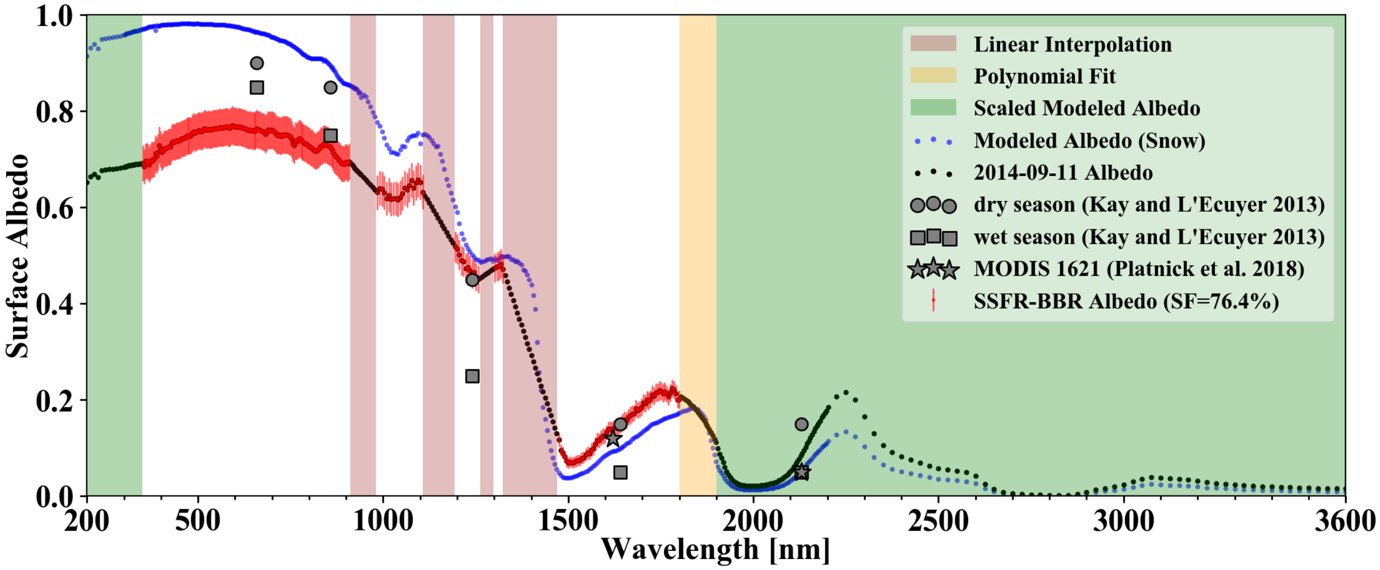

Figure 6: Spectral surface albedo (black) along with their uncertainties used in the RTM for the 2014-09-11 calculations. The spectral albedo uses the SSFR-BBR derived albedo with *SF*=76.4% (red) except for the wavelength ranges marked (1) in green: replaced by scaled modeled snow albedo (blue); (2) in red (gas absorption bands): linear interpolation; and (3) in yellow (1800nm to 1900nm): polynomial fit using SSFR-BBR derived albedo from 1650nm to 1800nm.

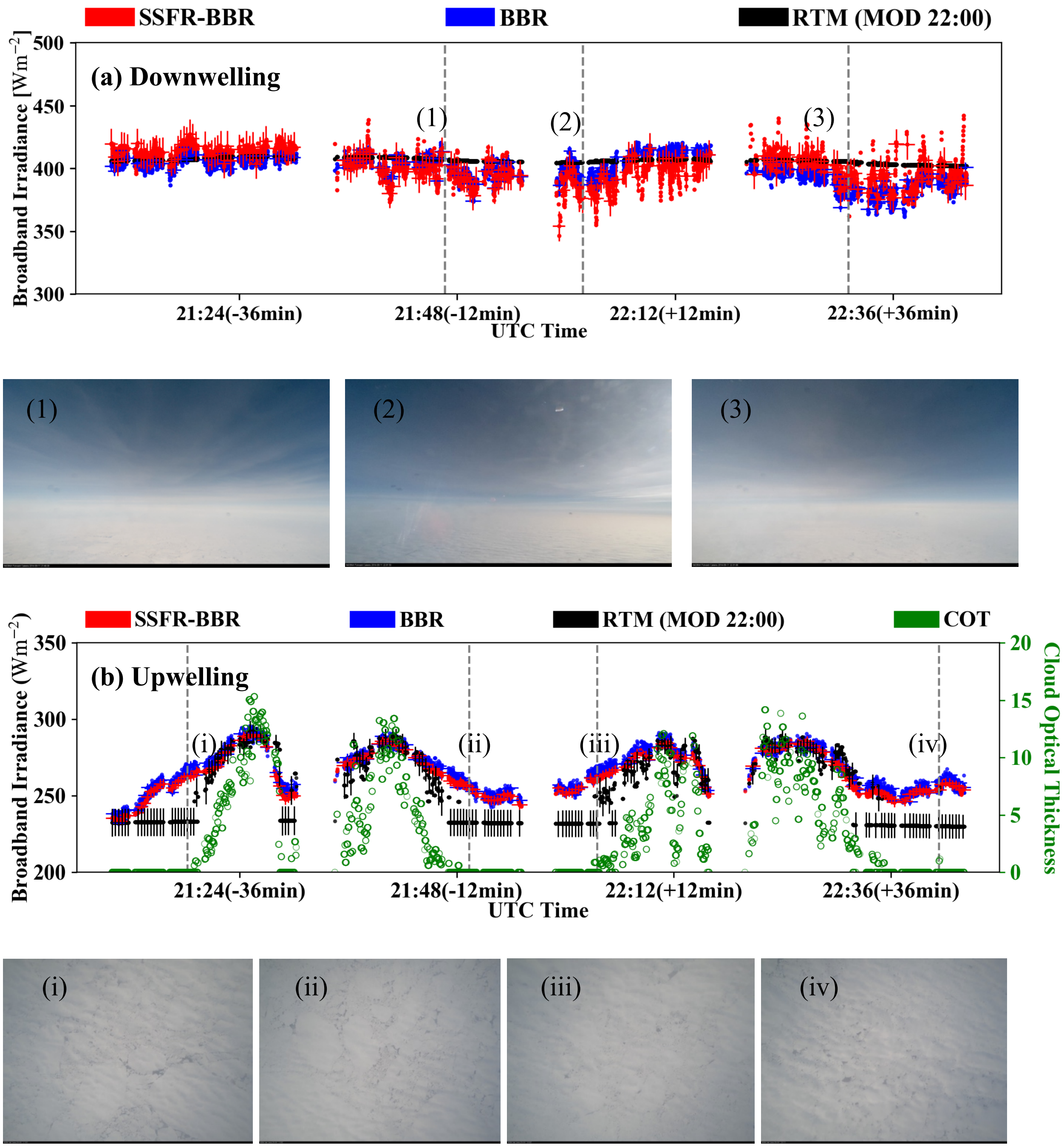

Figure 7. Broadband (a) downwelling and (b) upwelling irradiance from SSFR-BBR, BBR, and MODIS-COPs (Terra MODIS at 22:00) based RTM calculations on 11 September (above-clouds) along with their uncertainties. The observed irradiances include a horizontal error bar (indicating the size of the SSFR-BBR FOV) in addition to the vertical error bar (indicating the uncertainty of SSFR-BBR irradiance). The cloud optical thickness from MODIS is indicated in green. The average cloud optical thinness is 6.03. The forward camera images are provided at (1) 21:46:39, (2) 22:01:53, and (3) 22:31:05. The nadir camera images are provided at (i) 21:18:15, (ii) 21:49:22, (iii) 22:03:28, and (iv) 22:41:18 UTC. The time differences between aircraft measurements and MODIS granule are indicated in the axis labels. The average flight altitude was 7 km and the average aircraft ground speed was 150 m/s.

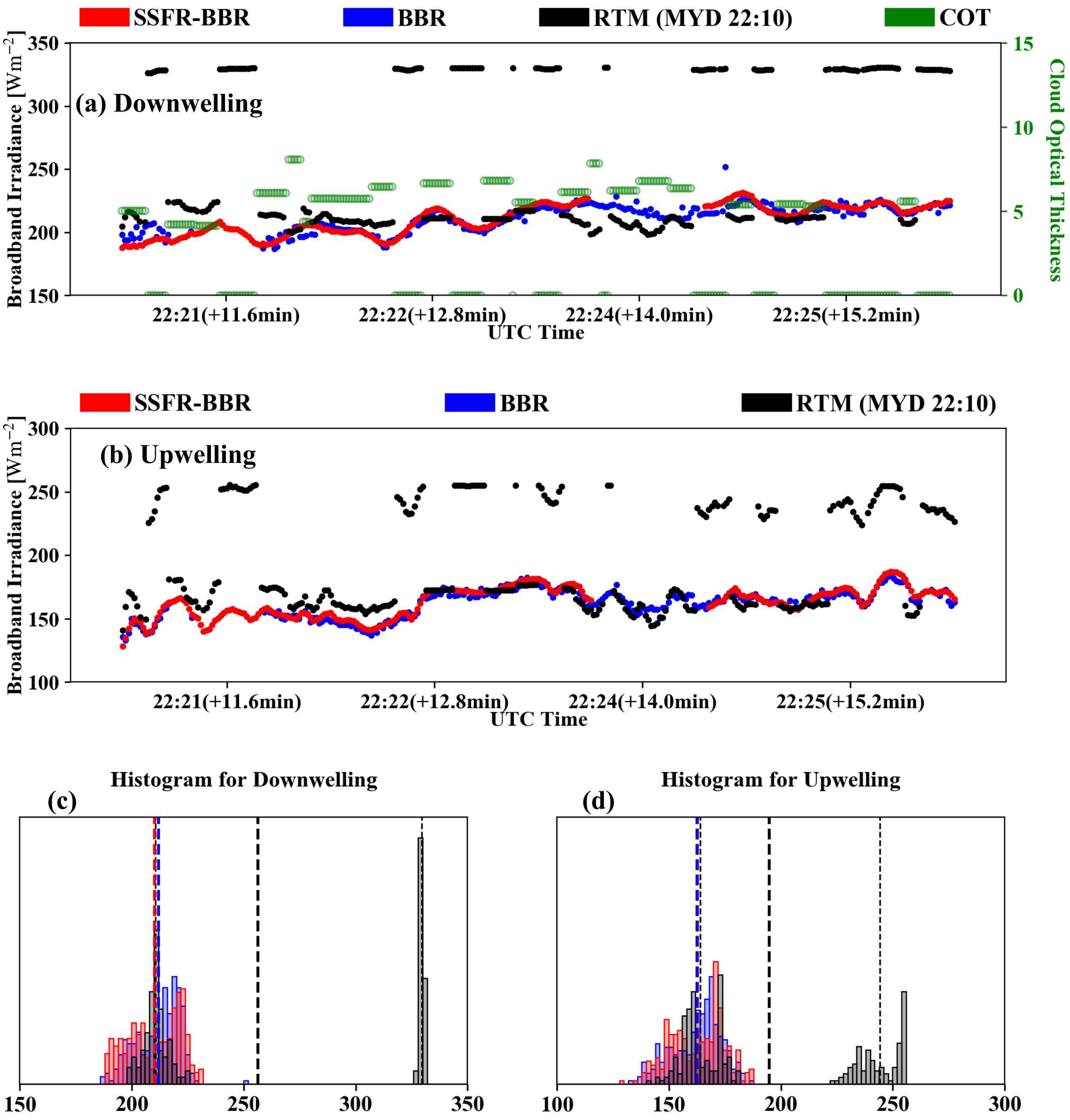
🟥 SSFR-BBR
🟦 BBR
⬛ RTM (MYD 22:10)
🟩 COT
(a) Downwelling
Broadband Irradiance [Wm^{-2}]
Cloud Optical Thickness
350
300
250
200
150
15
10
5
0
22:21(+11.6min)
22:22(+12.8min)
22:24(+14.0min)
22:25(+15.2min)
UTC Time
🟥 SSFR-BBR
🟦 BBR
⬛ RTM (MYD 22:10)
(b) Upwelling
Broadband Irradiance [Wm^{-2}]
300
250
200
150
100
22:21(+11.6min)
22:22(+12.8min)
22:24(+14.0min)
22:25(+15.2min)
UTC Time
Histogram for Downwelling
(c)
150
200
250
300
350
Histogram for Upwelling
(d)
100
150
200
250
300

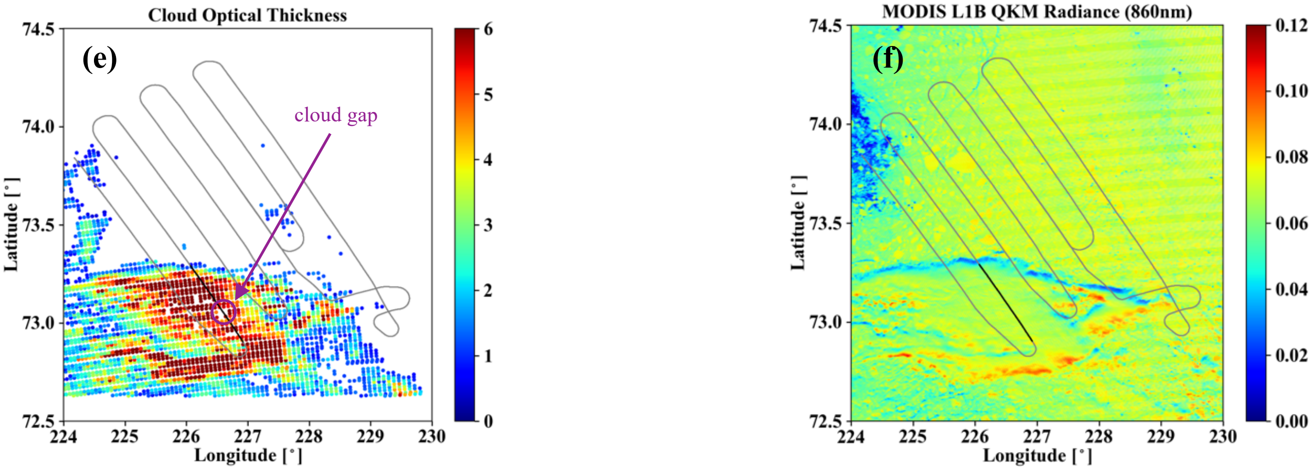

Figure 8. Broadband (a) downwelling and (b) upwelling irradiance from SSFR-BBR, BBR, and MODIS-COPs (Aqua MODIS at 22:10) based RTM calculations on 13 September (below-clouds) and (c) and (d) the histograms. The time difference between aircraft measurements and MODIS granule is indicated in the axis labels. In the histograms, the mean of BBR, SSFR-BBR, and RTM calculations are indicated by the thick dashed lines. The mean is calculated for each of the two modes in RTM calculations and indicated by the thin dashed lines. In addition, the field of cloud optical thickness and radiance at 860 nm from MODIS are provided in (e) and (f). On the map, the black line indicates the flight track studied in (a) – (d). The average flight altitude was 235 m, and the average aircraft ground speed was 106 m/s.

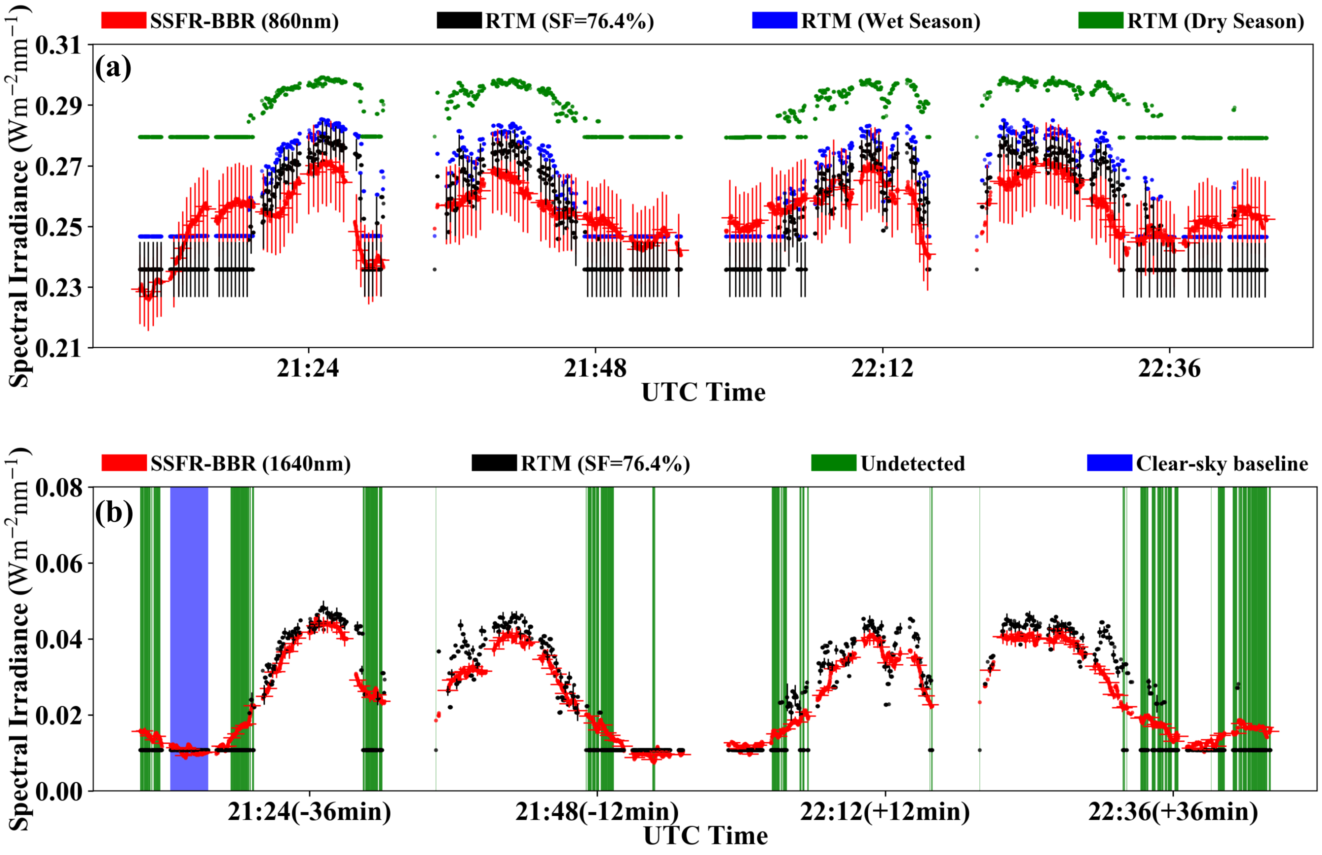

Figure 9. Spectral upwelling irradiance at 860nm (panel a) and 1640nm (panel b) from SSFR-BBR (red) and MODIS-COPs based RTM calculations using "13 September surface albedo" with *SF*=76.4% (black) on 11 September. In addition, calculations with climatological snow albedos are shown in panel (a) (Arctic wet season: 0.75; Arctic dry season: 0.85). The time periods where clouds were not detected are marked in green in panel (b). The clear-sky period that was used to determine the snow fraction is highlighted in blue in panel (b). The uncertainties of the spectral irradiances are indicated as vertical error bars, and the horizontal error bars correspond to the radiometer FOV as in Figure 7. Both need to be considered to identify undetected clouds.

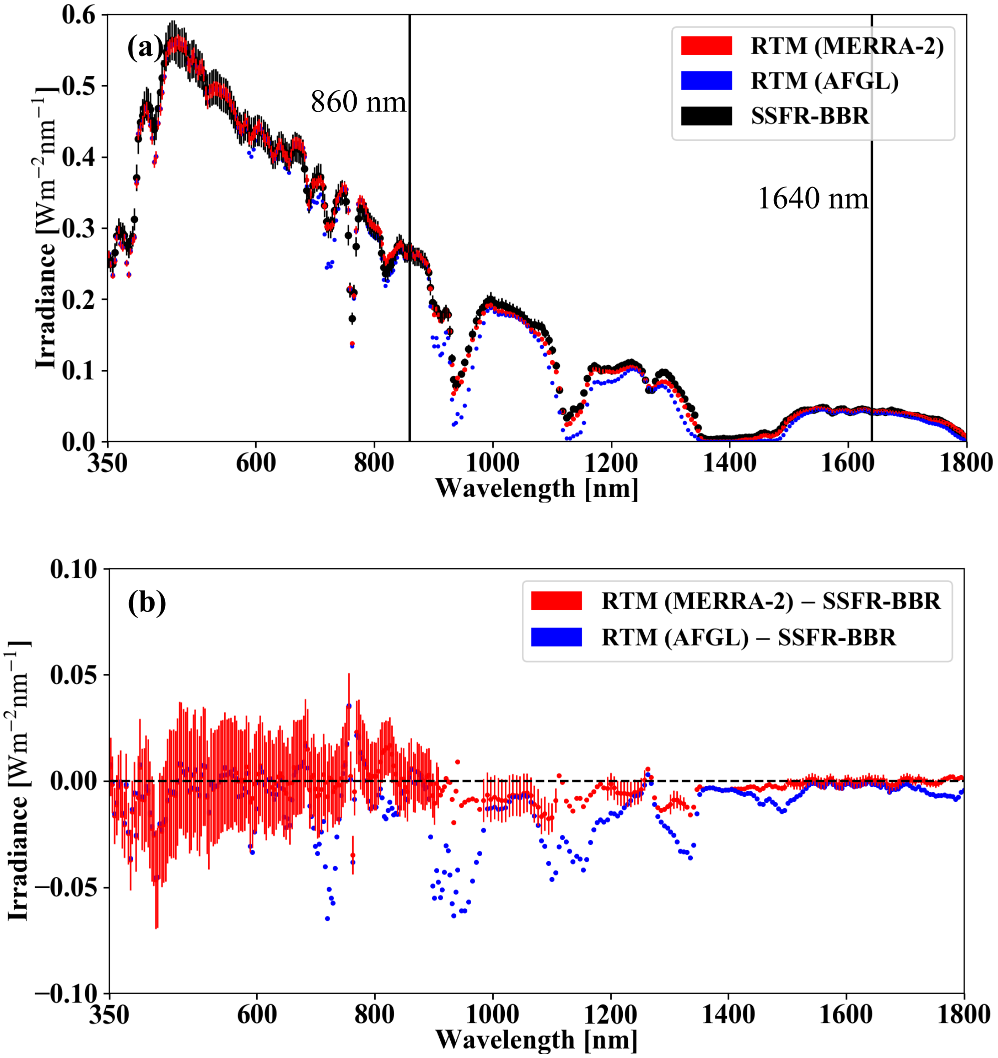

Figure 10. (a) Spectral upwelling irradiance from SSFR-BBR (black) and MODIS-COPs based RTM calculations with atmospheric profiles from MERRA-2 (red) and with AFGL subarctic summer climatology (blue) at 21:24 UTC on 11 September. (b) Irradiance difference between RTM and SSFR-BBR. The uncertainty of the SSFR-BBR irradiance is indicated as error bars (for one spectrum only).

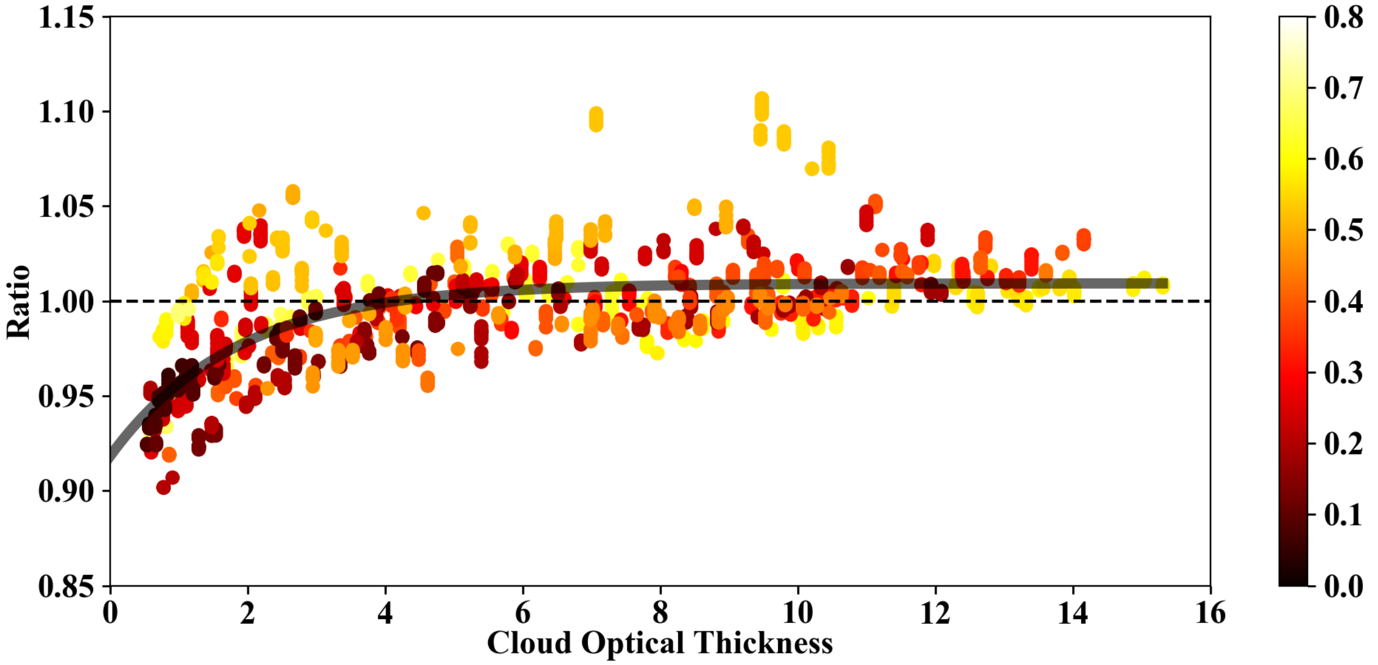

Figure 11. Ratio (RTM/SSFR-BBR) of upwelling broadband irradiance as a function of cloud optical thickness from MODIS "1621" cloud product on 11 September. The time differences between aircraft measurements and MODIS granule (unit: hour) is color-coded. The black curve is an exponentially fitted line using $r = a - e^{b \cdot COT + c}$, where $a = 1.0093$, $b = -0.5464$, and $c = -2.3954$.

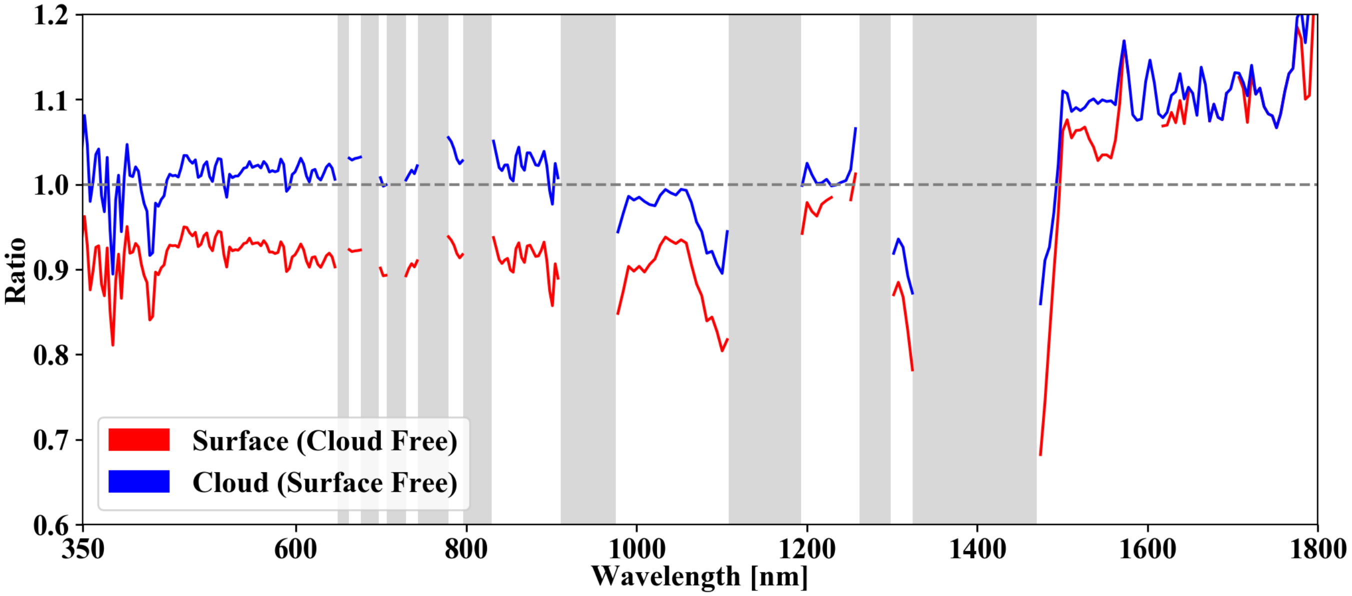

Figure 12. The spectrum of ratio when $COT = 0$ (red, indicating cloud free) and when $COT = \infty$ (blue, indicating surface free) for wavelengths range from 350 nm to 1800 nm. The gas absorption bands are indicated in gray. Ratios at the gas absorption bands are excluded.

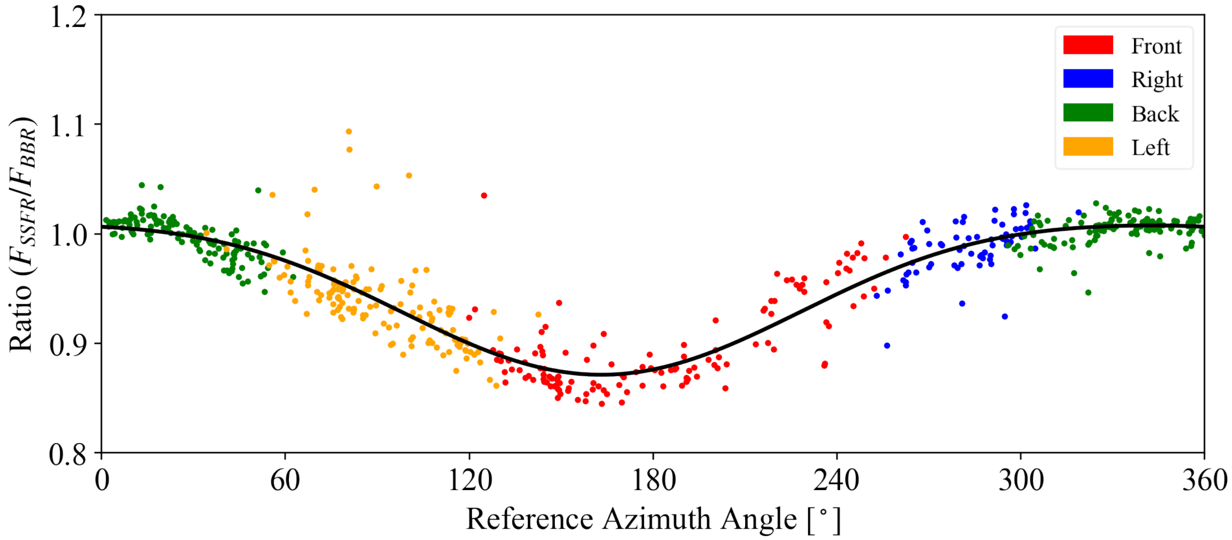

Figure A1: Ratio between spectrally integrated SSFR downwelling irradiance and broadband downwelling irradiance from BBR as a function of reference azimuth angle (solar azimuth position with respect to the sensor, 0 degree pointing north) during 1:00 UTC – 1:36 UTC on 2014-10-03. The relative positions of the sun with respect to the aircraft are indicated by different colors. The 5 black curve is a fitted function using a second order Fourier series.

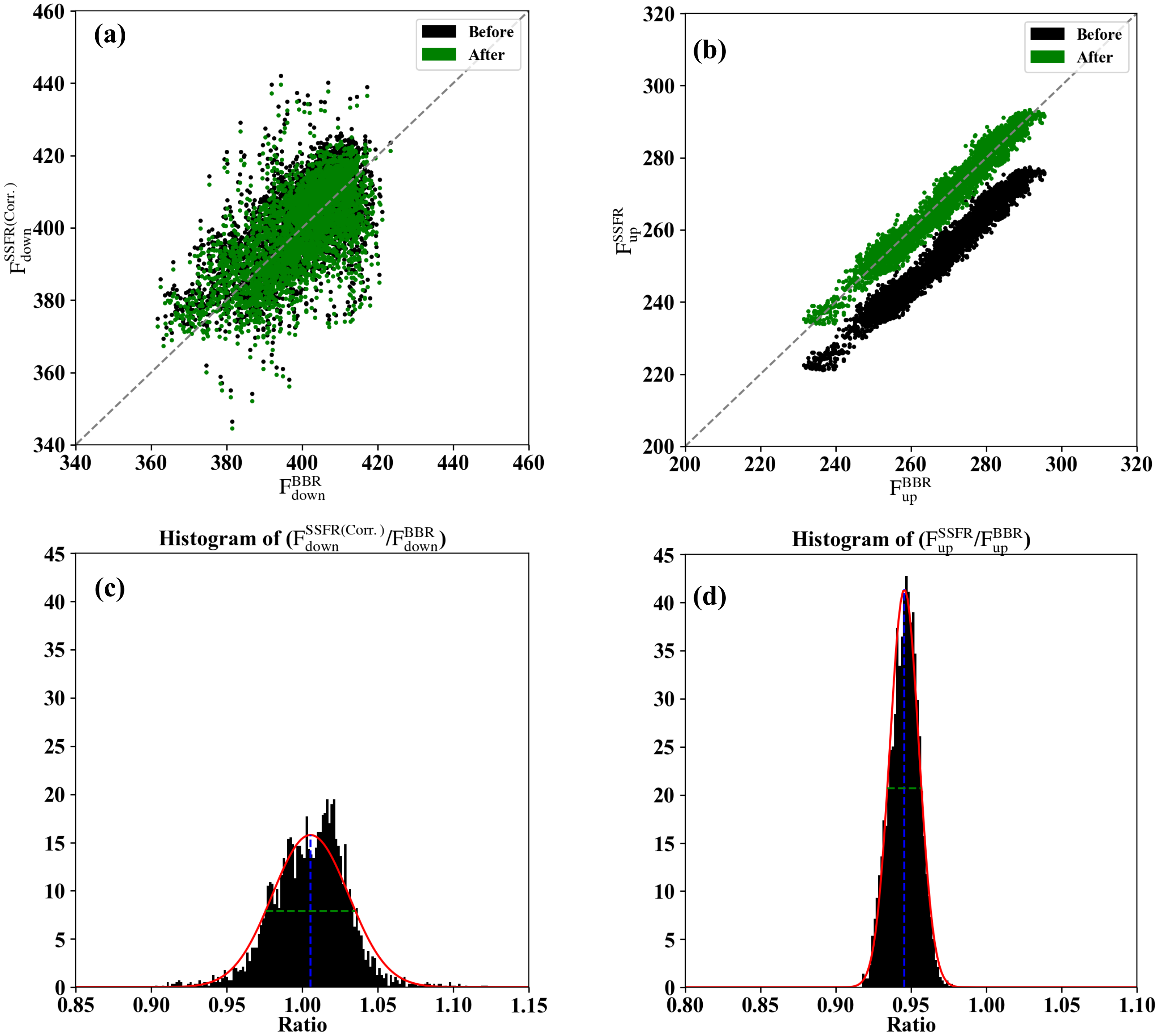

Figure A2: SSFR integrated broadband irradiance versus BBR broadband irradiance (a: downwelling; b: upwelling) and the histograms of the ratio of SSFR integrated broadband irradiance to BBR broadband irradiance (c and d) for the “0911-above-cloud” case. The mean and the full width half maximum of the Gaussian distribution of the ratio are indicated as blue and green dashed lines in the histogram plots. The SSFR-BBR data (SSFR after applying the scale factor as indicated by the blue dashed line) versus BBR is indicated in green in (a) and (b).

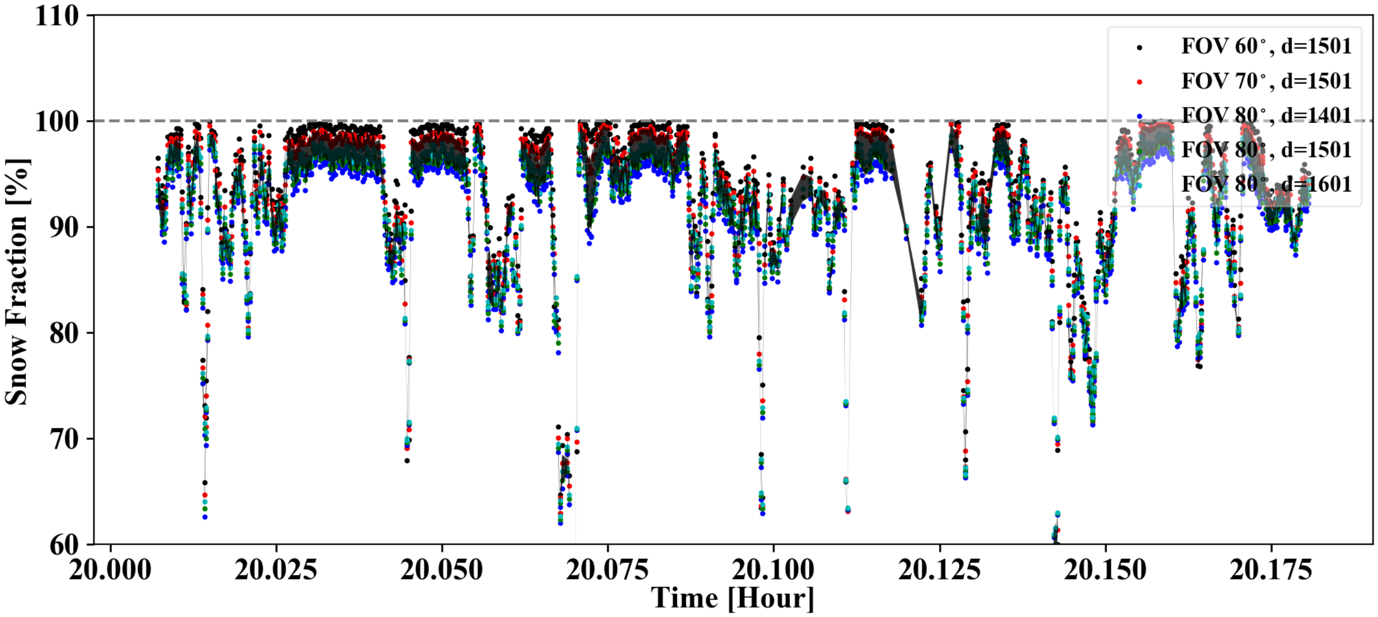

Figure A3: Snow fraction estimated using different FOV angles and subdomain sizes in the adaptive thresholding. The standard deviation of the 5 sets of snow fraction is shaded in black.